Final Report

Project Title:	Novel Approaches to Wide Bandgap $CuInSe_2$-based Absorbers	
Date of Report:	April 4, 2011	
Recipient:	University of Delaware	
Award Number:	DE-FC36-08GO18019	
Working Partners:	University of Oregon	
Cost-Sharing Partners:	University of Oregon	
Contacts:	William N. Shafarman Phone: 302-831-6215 Fax: 302-831-6226 Email: wns@udel.edu	Paula Newton Phone: 302-831-6221 Fax: 302-831-6226 Email: pnewton@udel.edu
DOE Project Team:	Contract Officer/Manager Project Officer/ Manager Project Monitor	Andrea Lucero Jim Payne Sven Nuesken

I. Introduction

The objective is this project "Novel Approaches to Wide Bandgap $CuInSe_2$-based Absorbers" was the development of high performance wide bandgap solar cells based on thin film alloys of $CuInSe_2$ to relax constraints on module design and enable tandem solar cell structures. Specific objectives of the research project were: 1) to develop the processes and materials required to improve the performance of wide bandgap thin film solar cells based on alloys of $CuInSe_2$, and 2) to provide the fundamental science and engineering basis for the material, electronic, and device properties required to effectively apply these processes and materials to commercial manufacture.

This project has addressed the goals of the Solar Energy Technologies Program for Next Generation PV by developing technology needed for higher thin film module efficiency as a means to reduce costs. $CuInSe_2$-based photovoltaics have established the highest efficiencies of the thin film materials at both the cell and module scales and many companies are currently developing manufacturing processes for commercialization. In the highest efficiency cells and modules, the optical bandgap, a function of the $CuInSe_2$-based alloy composition, is relatively low compared to the optimum match to the solar spectrum. Wider bandgap alloys of $CuInSe_2$ produce higher cell voltage which can improve module performance and enable the development of tandem solar cells to boost the overall efficiency. However, in previous efforts with wide bandgap alloys incorporating high Ga content, S or Al, the conversion efficiency decreases with increasing bandgap.

This project has been conducted in three tasks to pursue improved performance of solar cells using $CuInSe_2$-based absorber materials with bandgaps in the range of 1.4 to 1.8 eV. In the first task, different I-III-VI_2 chalcopyrite alloys are being deposited, characterized and incorporated into devices optimized for high performance. Efforts focused on $(AgCu)(InGa)Se_2$ pentenary thin films deposited by elemental co-evaporation which gives the broadest range of control of composition and material properties. This alloy has a lower melting temperature than Ag-free, Cu-based chalcopyrite compounds, which may enable films to be formed with lower defect densities. The second task investigated post-deposition processing of the $CuInSe_2$-alloy films using pulsed laser treatments and thermal annealing to control defect structure and electronic properties in the films. The third task investigated the electronic properties of the materials using advanced characterization of working solar cells to allow direct comparisons between electronic properties and device performance with deposition parameters and material properties.

This report describes the approaches taken in this project to develop and understand wide bandgap chalcopyrite materials and solar cells. A brief background to these approaches is provided in section II. Section III provides a description of the film deposition, solar cell fabrication, and basic characterization approaches used. More detailed descriptions of some characterization methods are coupled with the results. Section IV describes $(AgCu)(InGa)Se_2$ film processing and materials characterization including detailed structural and optical characterization. Solar cell results using $(AgCu)(InGa)Se_2$ absorber layers with a broad range of compositions and different deposition processes are described in Section V. Characterization of the electronic properties based on detailed application of capacitance-based methods is described in section VI. Finally, process descriptions and results of laser and thermal experiments are

presented in Section VII and a summary in section VIII. A list of publications to date resulting from work on this project is listed in Appendix I. Additional publications are still in preparation. And a list of contributors to this project at the University of Delaware and the University of Oregon is listed in Appendix II.

II. Background

High efficiency $Cu(InGa)Se_2$ based thin film solar cells typically have absorber layers with $[Ga]/[In+Ga] \approx 0.25$ and a bandgap (E_g) of ≈ 1.15 eV [i]. Wider bandgap absorber layers are desirable due to reduced losses related to the trade-off between higher voltage and lower current at maximum power. The resulting reduction in power loss, proportional to I^2R, can be used to either increase the module's active area by increasing the spacing between interconnects or grid lines, or to decrease the optical absorption in the transparent conduction layers since they can tolerate greater resistance. Wider band gap gives a lower coefficient of temperature for the device or module output power [ii], which will improve performance at the elevated temperatures experienced in most real terrestrial applications. Finally, improved wide band gap devices are necessary to enable a next generation $Cu(InGa)Se_2$ based device using a tandem or multijunction configuration [iii].

The chalcopyrite $CuInSe_2$ material system provides several options for alloying the film to increase the bandgap with previous efforts focused on high Ga substitution or alloying with S, or Al [1]. However, in all cases, the efficiency decreases when the alloy bandgap is greater than ~ 1.3 eV. Alloying with silver to form $(AgCu)(InGa)Se_2$ has the potential advantage of increasing the bandgap while also decreasing the melting temperature of the material [iv], as shown in Figure 1. This might enable the growth of films with reduced structural disorder and defects and, consequently, improved device performance.

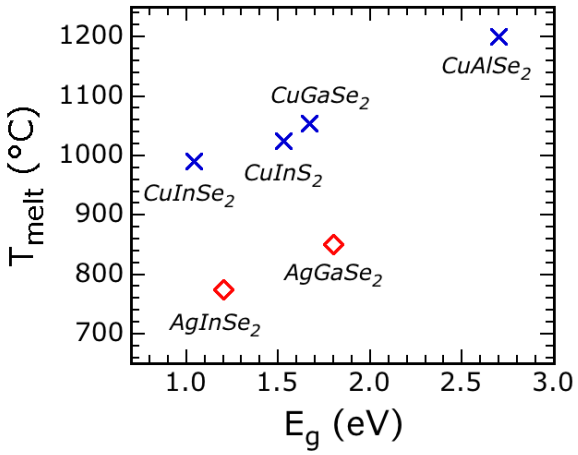

Figure 1. Melting temperature and bandgap of Cu- and Ag-based chalcopyrite alloys.

With all wide bandgap $CuInSe_2$-alloy solar cells, the performance is believed to be limited by recombination through defects in the absorber layer. One means to reduce the defects in materials is with post-deposition processes including laser annealing or rapid thermal annealing

(RTA). These approaches enable high effective surface temperatures with low overall temperature budgets that may improve material quality in the critical region of the $Cu(InGa)Se_2$ layer. Both laser annealing [v] and rapid thermal annealing [vi,vii] have been previously shown to improve the performance on non-optimal $Cu(InGa)Se_2$ devices.

III. Experimental Description

$Cu(InGa)Se_2$ and $(AgCu)(InGa)Se_2$ thin films were deposited by co-evaporation from elemental effusion sources in a bell jar system at IEC. The effusion source design developed at IEC for controlled evaporation of Cu, In, and Ga was utilized successfully for Ag evaporation. In previous work at IEC on different alloys it was found this source, fabricated using boron nitride, could not be used for evaporation of Al or S. With Ag controlled effusion rates were obtained over the full flux range needed to deposit a side range of $(AgCu)(InGa)Se_2$ film compositions. For all the evaporation sources the fluxes are controlled using a flux-temperature calibration taking advantage of the stability and reproducibility of the IEC effusion source design.

$(AgCu)(InGa)Se_2$ films were deposited with compositions spanning the complete range from $0 \leq x \leq 1$ and $0 \leq w \leq 1$ where $x \equiv [Ga]/[In+Ga]$ and $w \equiv [Ag]/[Ag+Cu]$. The films were deposited on Mo-coated soda lime glass (SLG) substrates. Two different evaporation processes were primarily used. The first is a single-stage deposition process in which all source temperatures are time-invariant throughout the deposition so all fluxes at the substrate are constant. This typically forms films with nominally homogeneous through-film composition and no bandgap gradients. The substrate temperature is normally $T_{SS} = 550°C$ and the total deposition time 60 min. The second process was a three-stage evaporation similar to that used to deposit the $Cu(InGa)Se_2$ films in the highest efficiency thin film solar cells. The three-stage process consists of: 1) deposition of In/Ga/Se typically comprising the majority of Ga and In that will ultimately be delivered to the film; 2) deposition of Cu/(Ag)/Se until the film possesses a stoichiometric excess of group I elements; and 3) a second In/Ga/Se deposition to bring the film back to group I deficiency. Three-stage depositions were done with $T_{SS} = 400$ or 550°C in the first stage and 550°C for the latter stages. With both processes, typical films were 1.8 – 2.0 μm thick and had an overall Cu+Ag deficient composition [$(Ag+Cu)/(In+Ga) \approx 0.8 – 0.9$].

A number of methods were used in this work to characterize the material properties. These include:

- Determination of film composition by energy dispersive X-ray spectroscopy (EDS) carried out at 20kV electron accelerating. This was performed in an SEM which was also used for characterization of film morphology.
- Structural characterization by X-ray diffraction (XRD) using a Philips PW1729 X-ray diffractometer with a Cu Kα X-ray source and Bragg-Brentano focusing geometry. In some cases this was complemented by glancing angle XRD (GIXRD).
- Optical transmission and reflection measurements using a Perkin-Elmer Lambda 750 UV/Vis/NIR spectrophotometer equipped with an integrating sphere. For optical measurements films were deposited on bare SLG substrates as companion samples in the same run as SLG/Mo substrates for devices and other measurements.

- X-ray photoelectron spectroscopy (XPS) measurements using a Physical Electronics instrument with a monochromatic Al Kα x-ray excitation under the applied voltage of 20 kV with an Ar^+ ion gun (2 keV) for etching to perform depth profiling.
- Auger electron spectroscopy (AES) to determine compositional depth profiles. Measurements were performed by Glenn Teeter at NREL.

The primary electrical characterization was done on completed solar cells. These were fabricated with structure glass/Mo/Cu(InGa)$(SeS)_2$/CdS/ZnO/ITO/(Ni-Al grid) with 0.47 cm^2 cells delineated by mechanical scribing. The substrate is 1.5 mm thick soda lime glass. The Mo is 0.7 μm thick and deposited by dc sputtering. The CdS emitter layer is deposited by chemical bath deposition with thickness ~ 40 nm. ZnO and ITO layers are deposited by rf sputtering with no substrate heating. The ZnO is 50 nm thick. It is undoped with resistivity ρ = 1 - 10 Ω-cm. The ITO layer is 150 nm thick with $\rho = 3 \times 10^{-4}$ Ω-cm. Ni (100 nm)/Al (3 μm) grids are evaporated through an aperture mask with total shading ~ 4%. While most cells in this report had no antireflection layer, In a few instances as noted a 110 nm thick MgF_2 AR layer was deposited by electron beam evaporation.

Standard device characterization included J-V measurement under 100 mW/cm^2 AM1.5 illumination at 25°C. Quantum efficiency measurements were performed with and without white light bias and at different voltage biases. More advanced characterization will be described in section VI.

IV. (AgCu)(InGa)Se_2 thin films

(AgCu)(InGa)Se_2 Deposition

(AgCu)(InGa)Se_2 films were deposited over a broad range of compositions by both single-stage and three-stage evaporation processes. For Cu(InGa)Se_2 films the three-stage produces results in films with through-film composition gradients characterized by a decrease in [Ga]/[In+Ga] from the back of the film until a "notch" near the front and then an increase in [Ga]/[In+Ga] to the front surface [viii].

The effect of Ag incorporation on the through-film composition was studied for both processes. AES depth profiles of four films with high Ga content ($x \approx 0.8$), listed in Table I, are shown in Figures 2 – 6. The single-stage films exhibit nearly invariant composition through the depth of the films, with small gradients that may result from variations in flux during deposition. The three-stage films display the characteristic Ga "notch" previously reported for Cu(InGa)Se_2 films deposited by a three-stage process [ix]. In all of the samples, the Ag/(Ag+Cu) ratio appears roughly constant through the depth of the film, with the possible exception of the sample with x = 0.2 and w = 0.3 in which the Ag content may be slightly tracking the In content.

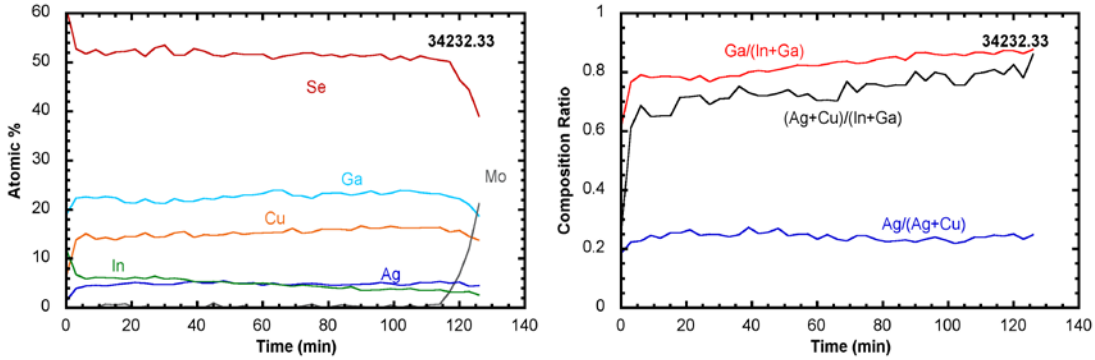

Figure 2. Auger depth profiles for single-stage absorber layer with x = 0.8 and w = 0.3.

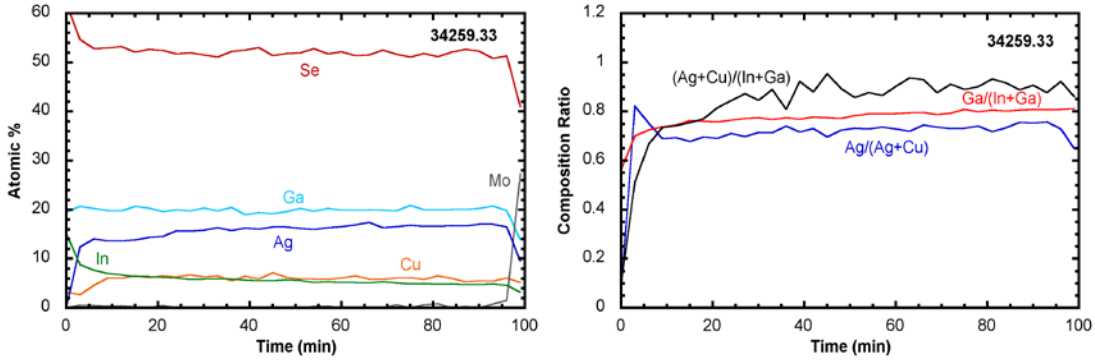

Figure 3. Auger depth profile for single-stage absorber layer with x = 0.8 and w = 0.8.

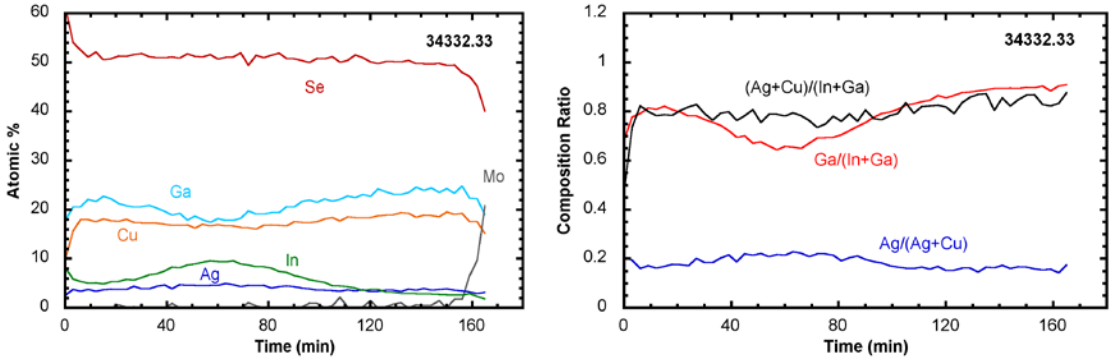

Figure 4. Auger depth profile for three-stage absorber layer with x = 0.8 and w = 0.2.

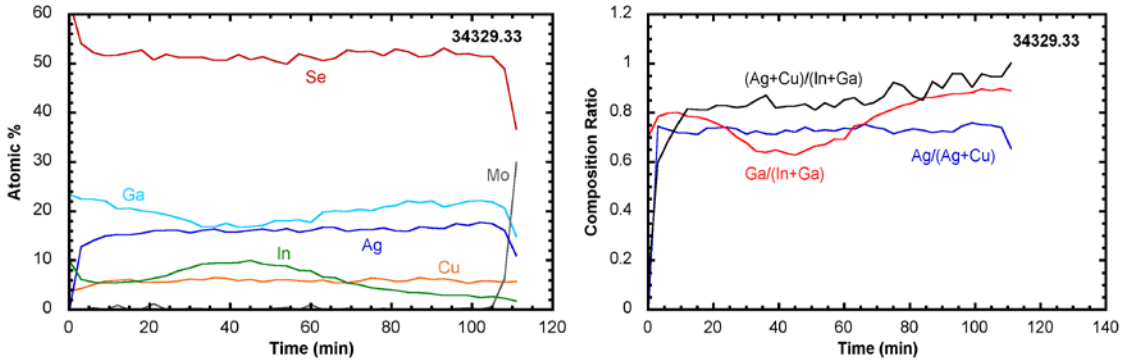

Figure 5. Auger depth profile for three-stage absorber layer with x = 0.8 and w = 0.8.

Table I. Composition by EDS of wide-bandgap (AgCu)(InGa)Se_2 absorber layers.

Process	*w*	*x*	$\frac{Ag+Cu}{In+Ga}$
Single-stage	0.30	0.81	0.79
Three-stage	0.76	0.81	0.86
Singe-stage	0.22	0.77	0.93
Three-stage	0.77	0.80	0.92

Films with high relative Ga content $x \geq 0.75$ can exhibit islanding due to lateral compositional segregation. Islanding in the deposition of $CuGaSe_2$ films has been previously observed [x] and was addressed by increasing the selenium delivery rate. A series of (AgCu)(InGa)Se_2 films with composition Ag/(Cu+Ag) = 0.75 and Ga/(In+Ga) = 0.8 were deposited with progressively increasing Se evaporation rate and are shown in Figure 6. The estimated selenium-to-metal incident flux ratios were assumed to be equal to the selenium-to-metal effusion rate ratios from the source bottles. The films deposited at Se-to-metal incident flux ratios below ~ 10 exhibit obvious islanding. EDS composition analysis is shown in Table II for the film deposited at Se-to-metal incident flux ratio of 5.4. The results suggest a chalcopyrite surface phase with composition very similar to the expected bulk composition, and an underlying Ga- and Se-rich phase such as Ga_2Se_3. Similar to previously observed results for the $CuGaSe_2$ system, increasing Se incident flux reduced the islanding.

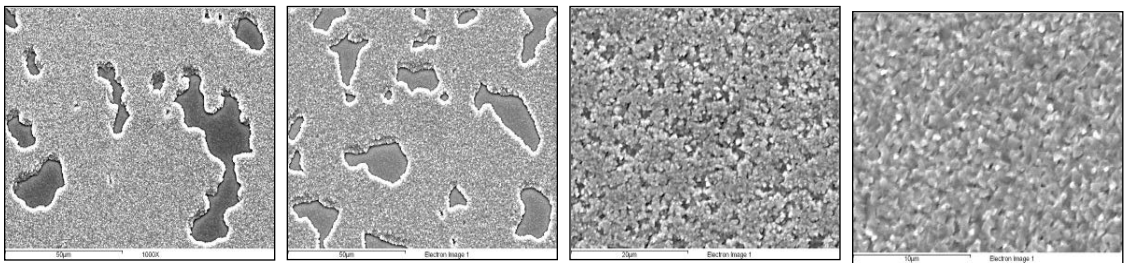

Figure 6. Single-stage (AgCu)(InGa)Se_2 films with composition *w* = 0.75 and *x* = 0.8 deposited with varying Se incident flux rates. Estimated selenium-to-metal incident flux ratios from left to right: 5.4 (scale bar = 50 μm), 9.2 (50 μm), 10.4 (20 μm), and 18.9 (10 μm).

Table II. Composition by EDS of segregated film with Se-to-metal incident flux ratio of 5.4 from Figure 6.

Element	Atomic concentration (%)	
	Raised surface (contiguous)	Sunken backplane (dispersed)
Ag	17.2	3.0
Cu	4.8	5.5
In	4.9	4.1
Ga	21.0	29.2
Se	52.2	57.9

$(AgCu)(InGa)Se_2$ films deposited using the single-stage process, with Se-to-metal ≥ 15 for high Ga films, were used for structural and optical characterization to avoid complications in the analysis due to the composition gradients.

Structure and Morphology

The phase behavior of the $(AgCu)(InGa)(TeSe)_2$ system has been previously studied by Avon et al. [xi1] A chalcopyrite-chalcopyrite miscibility gap was observed by XRD analysis of ampoule-synthesized $(AgCu)(InGa)Se_2$ polycrystal ingots in the approximate composition window $0.25 < w < 0.75$ and $0.25 < x < 1.0$ [xi]. There is no previous report of the structure of $(AgCu)(InGa)Se_2$ thin films so it was unknown whether such a gap would exist. The x-ray diffraction spectrum of a film with [Ga]/[In+Ga] = 0.50 and [Ag]/[Ag+Cu] = 0.46 is shown in Figure 7.

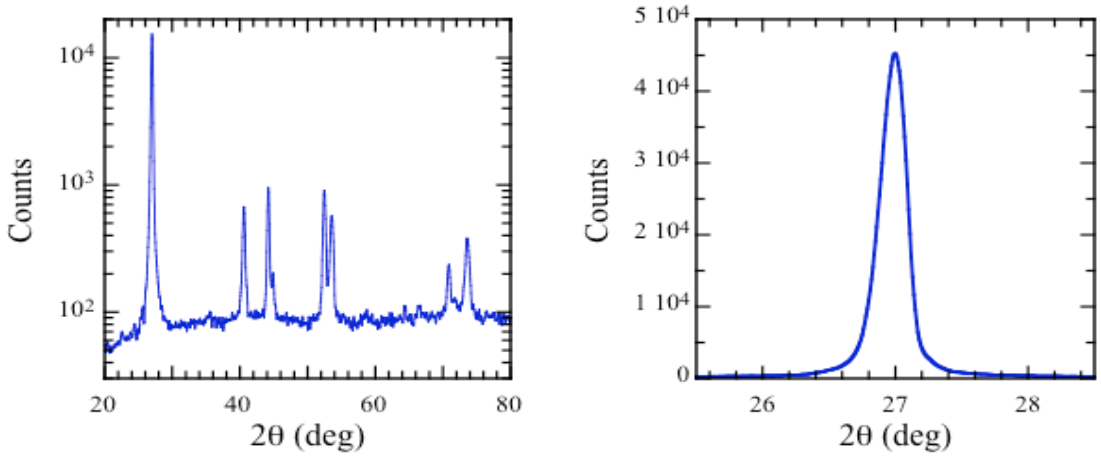

Figure 7. XRD full spectrum (left) and high resolution spectrum of the (112) peak for an $(AgCu)(InGa)Se_2$ film with $x \equiv [Ga]/[In+Ga] = 0.50$ and $w \equiv [Ag]/[Ag+Cu] = 0.46$ showing a single chalcopyrite phase.

This spectra shows a single chalcopyrite phase with no peak splitting or broadening. There is no evidence of phase separation which would cause a splitting of the (112) peak in particular. Similar behavior was observed over the entire composition range.

To further understand the effect of Ag alloying on the chalcopyrite structure, a set of 6 films with $x = 0.5$ and $0 \leq w \leq 1$ was characterized in detail [xii]. These films are listed in Table III and their XRD spectra are shown in Figure 8.

Table III. Compositions and lattice constants for $(AgCu)(InGa)Se_2$ thin film samples for structural characterization. A lower Figure of Merit (FoM) indicates a better determination of the lattice constant.

$\frac{Ag}{Ag+Cu}$	$\frac{Ag+Cu}{In+Ga}$	$\frac{Ga}{In+Ga}$	a_O (Å)	c_O (Å)	c/a	FoM
0	0.89	0.48	5.692	11.279	1.982	$4x10^{-5}$
0.14	0.86	0.49	5.733	11.287	1.969	$4x10^{-6}$
0.27	0.87	0.50	5.761	11.288	1.960	$3x10^{-5}$
0.48	0.94	0.50	5.875	11.368	1.935	$2x10^{-3}$
0.76	0.81	0.53	5.946	11.271	1.895	$2x10^{-4}$
1	0.95	0.52	6.061	11.239	1.854	$2x10^{-4}$

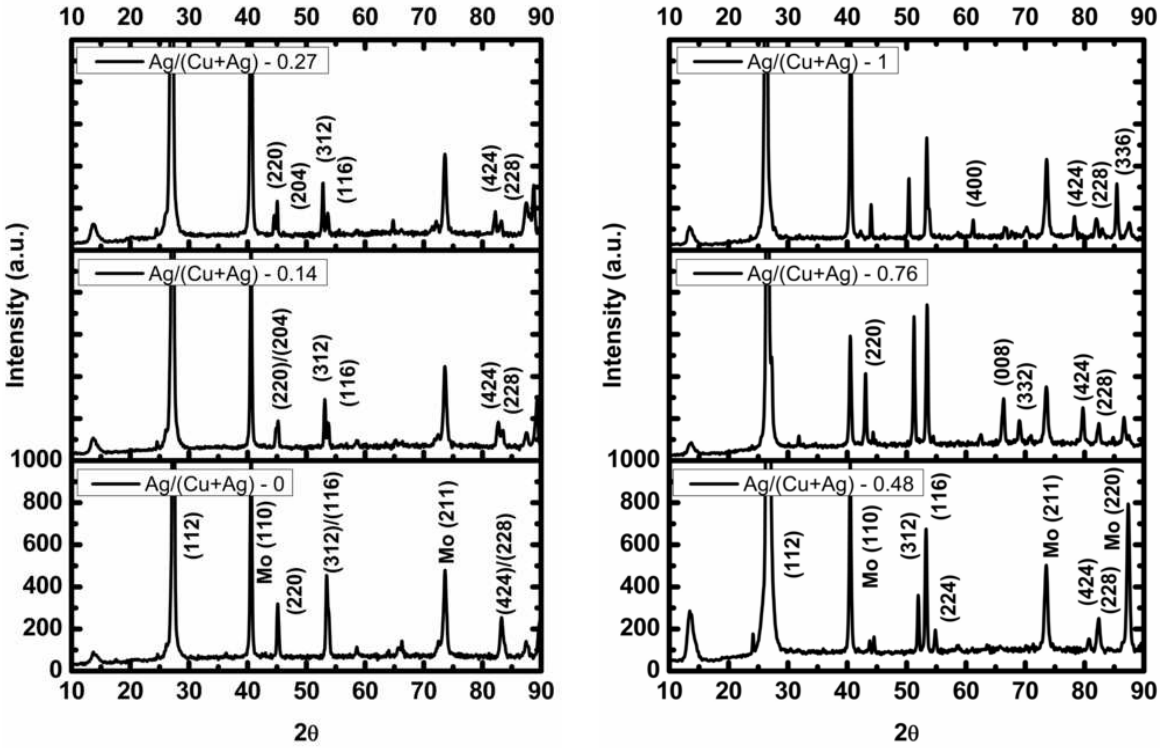

Figure 8. XRD patterns of films listed in Table III. The Intensity scale is 0 – 1000 for all compositions.

The XRD patterns in Figure 8 show a loss of degeneracy for certain reflections, such as the (220)/(204), (305)/(323), (424)/(228), etc. due to the increasing tetragonal distortion with increasing Ag content, leading to $c_o/a_o < 2$. Also, there is a general trend for an increase in the number of strong reflections (≥2x the signal-to-noise-ratio) as Ag is incorporated. For the samples with $w = 0$, 0.14, and 0.27 all reflections were assignable to either the chalcopyrite crystal structure (space group = 122) or Mo. A few reflections with low intensity, near the signal-to-noise threshold, were not assignable for the samples with $w = 0.48$, 0.76, and 1 suggesting the presence of secondary phases for these three samples. The presence of a $Ag(InGa)_5Se_8$ secondary

phase could not be confirmed for these samples due to an insufficient number of identifiable reflections.

Fine scans of the (112) reflections for the six samples are shown on a linear scale in Figure 9 and the shift in the (112) reflection to lower 2θ with the incorporation of Ag is evident. The (112) FWHM was determined from the (112) fine scans and shows a general decrease ($2\theta \approx 0.175 \rightarrow 2\theta \approx 0.135$) with an increase in Ag. This suggests that the structural quality of the films is increasing with Ag incorporation, although broadening due to compositional distribution or stress cannot be ruled out.

The lattice constants c_o and a_o of the chalcopyrite phase for the six samples were determined via the Cohen Method [xiii,xiv]. The results are shown in Figure 10 and listed above in Table III. The values for the a_o lattice parameter and the c_o/a_o ratio agree well with the published data determined from polycrystals [xi] over the limited data range for which single-phase behavior was observed. The a_o lattice parameter shows a nearly linear increase with composition, while the c_o and the c_o/a_o ratio shows a non-linear decrease with composition. The value for $w = 0.48$ is aberrant from the other data points and is not fully understood at this time. The $w = 0.48$ composition was redeposited and recharacterized, with the results confirming the initial observation.

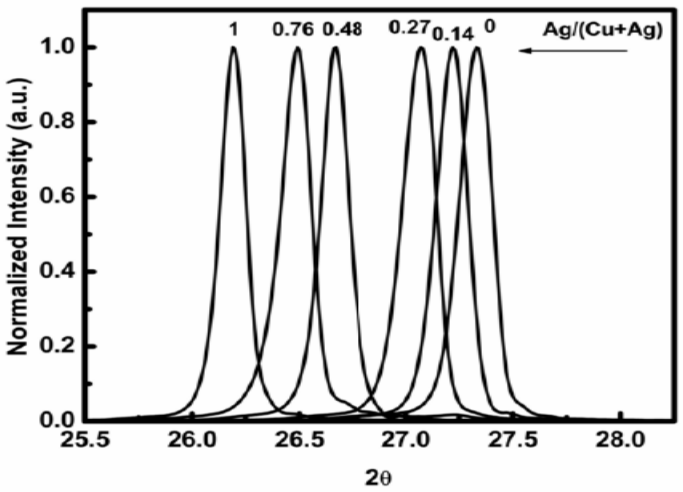

Figure 9. XRD (112) line profiles of the films listed in Table III.

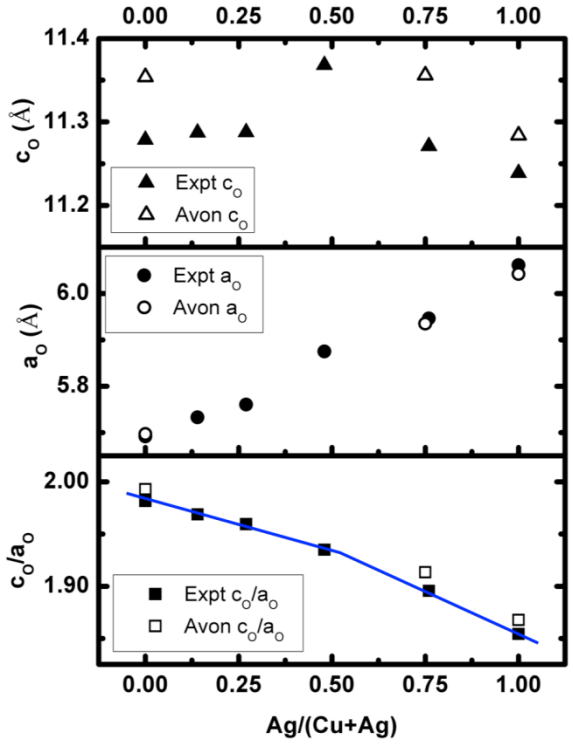

Figure 10. Lattice constants versus *w* for films in Table III compared to results on polycrystal ingots (Avon, et al. [6]).

Multiple factors might account for the differences between the film and bulk samples. The bulk polycrystals were grown by high temperature (~1000^{o}C) stoichiometric ampoule synthesis, with long anneal times [xi]. In comparison, we deposited group I (Cu+Ag) deficient thin films via co-thermal elemental evaporation at 550^{o}C, and cooled our samples to ambient temperatures in ~3 hours. The lower deposition temperature and comparatively quick cooling introduce the

possibility of metastable films. The use of thin films also raises the possibility that deposition on Mo-coated soda lime glass induces strain in the chalcopyrite film.

The effect of Ag addition on morphology and grain size has been characterized by atomic force microscopy. Figure 11 shows a set of (AgCu)$InSe_2$ films with increasing relative Ag content from $w = 0$ to 1. Each image shows a 10 x 10 µm area. The rms roughness values from these measurements are listed in Table IV. All of the films containing Ag have a more faceted morphology and smaller rms roughness than the $CuInSe_2$ film ($w = 0$). In addition, the grain size of the (AgCu)$InSe_2$ films appear to increase with increasing Ag content. A similar increase in apparent grain size was observed with increasing Ag for (AgCu)(InGa)Se_2 films with fixed relative Ga content, $x = 0.3$.

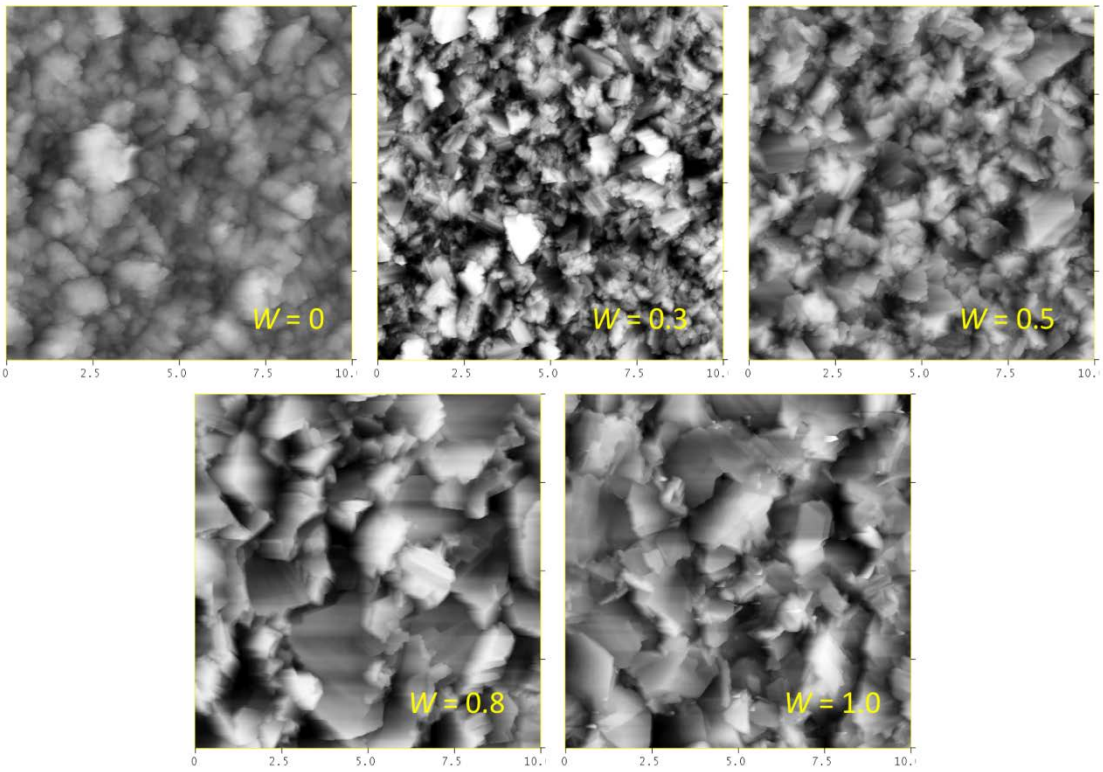

Figure 11. AFM images of (AgCu)$InSe_2$ films with increasing relative Ag content, $0 \leq w \leq 1$. Each image shows a 10 µm x 10 µm area.

Table IV. RMS roughness from AFM characterization of (AgCu)$InSe_2$ films with increasing Ag.

$\frac{Ag}{Ag+Cu}$	rms roughness (nm)
0	126
0.3	56
0.5	61
0.8	81
1.0	69

Optical characterization

$(AgCu)(InGa)Se_2$ films were grown on bare glass substrates for optical characterization. The normalized transmission [T/(1-R)] curves of 2 sets of films with $x = 0$ and 0.3 and $0 \leq w \leq 1$ are shown in Figure 12. The increase in bandgap with increasing w is seen in the shift of the transmission curves to lower wavelengths (higher energies). In each set of films, the transmission in the sub-bandgap energy range for the $Cu(InGa)Se_2$ ($w = 0$) sample has greater sub-band gap absorption (lower transmission) than any of the $(AgCu)(InGa)Se_2$ samples [xv]. Similar behavior is seen with higher Ga content. This suggests that the incorporation of Ag always reduces the density of sub-bandgap defects. In addition, the higher sub-bandgap transmission with Ga will be beneficial for top cell application in a tandem structure

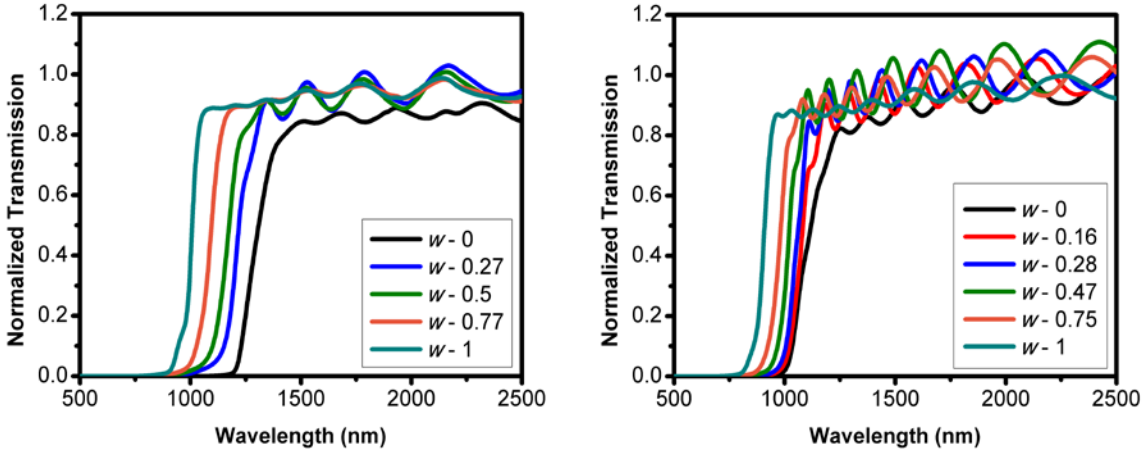

Figure 12. Normalized transmission T/(1-R) for $(AgCu)(InGa)Se_2$ films with $x = 0$ (left) and $x = 0.3$ (right) and varying Ag content w. In each case the sample with $w = 0$ (black) has lower transmission at sub-bandgap energies.

The optical bandgap was determined from the transmission and reflection data using a standard analytical procedure [xvi]. The absorption coefficient (α) was determined using

$$\alpha(\lambda,R,T) = \left(\frac{1}{d}\right) ln\left[\frac{(1-R)^2}{T}\right] \qquad (1)$$

where d is the sample thickness in cm and λ is the incident wavelength. Then E_g was determined by plotting $(\alpha E)^2$ vs. E and performing a linear fit of the data. This assumes that the fundamental optical transition is due to a direct allowed transition in all cases.

The bandgaps are shown in Figures 13 versus w with curves showing the polynomial fits for each set of films with fixed Ga fraction and in Figures 14 versus w with curves showing the polynomial fits for each set of films with fixed Ag fraction. Each curve determines the bowing parameter b, defined by :

$$E_g(x) = (1-x)E_g(0) + xE_g(1) - bx(1-x). \qquad (2)$$

The values of the bowing parameters are listed in Table V. For variation of w with fixed x, b = 0.2 for all values of x. For variation of *x* with fixed *w*, b varies from 0.04 to 0.2 with the larger values when *w* = 0.5 or 0.75.

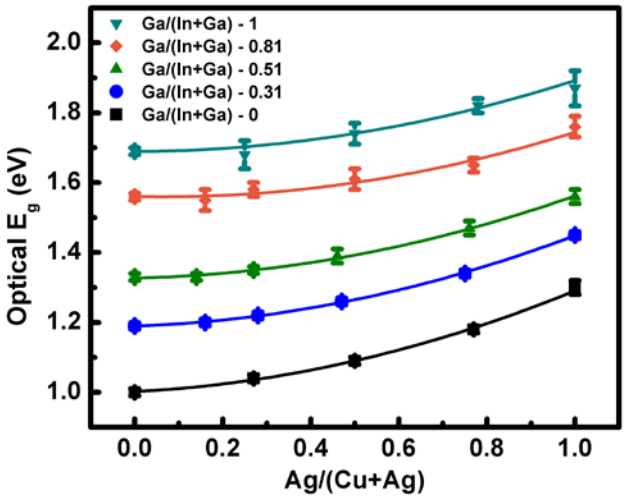

Figure 13. Bandgaps of (AgCu)(InGa)Se_2 films versus *w* with curves fit to give the bowing parameters in Table V.

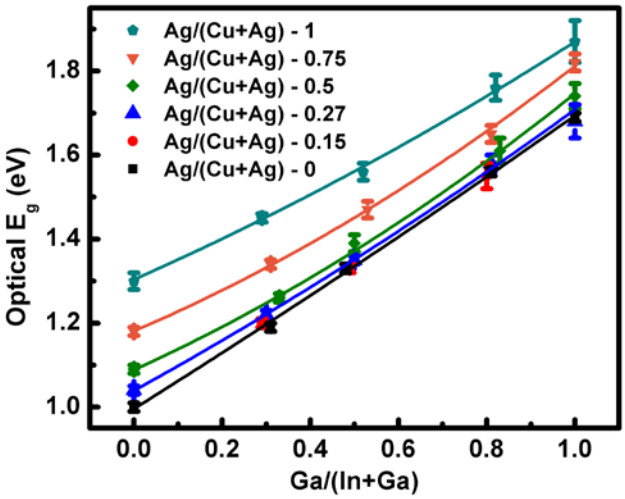

Figure 14. Bandgaps of (AgCu)(InGa)Se_2 films versus *x* with curves fit to give the bowing parameters in Table V.

Finally, a multi-variable linear regression of all the bandgaps was done to determine the following empirical formula to determine the bandgap at any composition:

$$E_g(x,w) = 0.08x^2 + 0.61x + 0.25w^2 + 0.03w - 0.11xw + 1.01 \text{ eV} \qquad (3)$$

Table V. Optical bowing parameters for (AgCu)(InGa)Se_2 films with respect to Ag fraction w (top) and Ga fraction x (bottom).

w	b	± standard Error
0	0.22	0.05
0.3	0.21	0.06
0.5	0.22	0.04
0.8	0.21	0.09
1	0.20	0.14

x	b	± standard error
0	0.04	0.04
0.27	0.09	0.07
0.5	0.18	0.07
0.75	0.18	0.06
1	0.10	0.10

V. (AgCu)(InGa)Se_2 devices and analysis

Solar cells were completed with a standard structure of SLG / Mo / (AgCu)(InGa)Se_2 / CdS / ZnO / ITO / grids and 0.47 cm^2 total area cells were delineated by mechanical scribing. All results are reported without the benefit of an anti-reflection layer.

Solar cells were fabricated in sets with fixed Ga fraction *x* and increasing Ag fraction *w*. V_{OC}, J_{SC}, FF and efficiency (η) are shown in Figure 15 for the best cell at each composition. In each set, V_{OC} increases with Ag addition as expected for increasing E_g. The V_{OC} increase is sub-linear with increasing Ga fraction or bandgap, as with Cu(InGa)Se_2 and other alloys [xvii,xviii]. However, greater improvement in V_{OC} with increasing Ag addition is demonstrated by the sets with $x = 0.65$, with E_g increasing from 1.4 to 1.5 eV and $x = 0.8$ and E_g from 1.55 – 1.66 eV. In these sample sets with higher Ga fraction, J_{SC} does not decrease with increasing bandgap indicative of improved current collection.

The highest values of FF are achieved with Ag alloying and x = 0.3 or 0.5. Values of FF = 80% are particularly noteworthy because there is no bandgap gradient to assist current collection as is created in Cu(InGa)Se_2 deposited with a 3-step evaporation process. This high FF cannot be attributed to changes in parasitic losses such as shunt or series resistances. Instead, it may be further indication of improved minority carrier collection length. The efficiencies with Ag alloying are, within the experimental spread, the same for the samples with x = 0.3 and 0.5 despite the increased E_g and V_{OC} with higher Ga. In devices without Ag, η decreased from 16 to 15 %.

Overall, the solar cell results show that Ag alloying can produce improved device performance. In particular, while the bandgap in the highest efficiency Cu(InGa)Se_2 cells is ~ 1.15 eV, Ag alloying allows the bandgap to be increased to 1.3 eV with an increase of up to 100 mV in V_{OC}

and no loss in device efficiency. With E_g > 1.5 eV, V_{OC}, *FF*, and efficiency all increase with increasing Ag content.

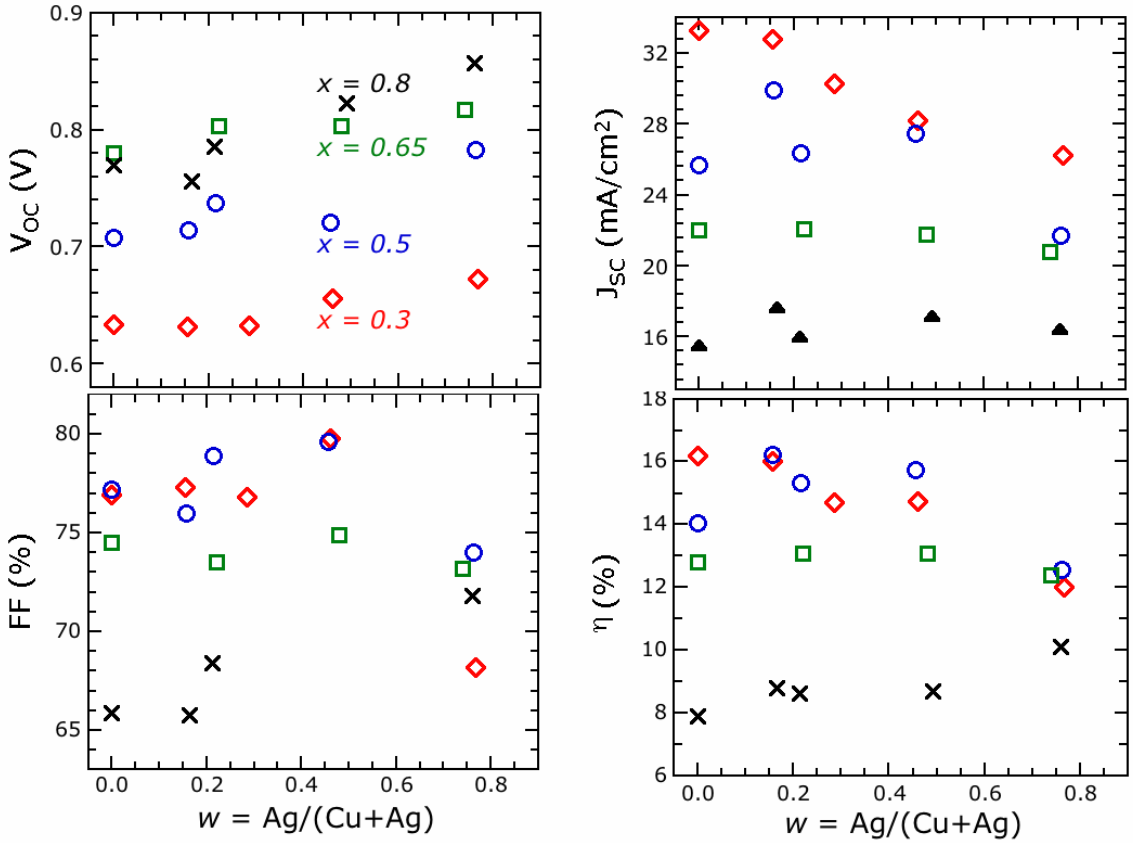

Figure 15. V_{OC}, J_{SC} FF, and efficiency vs. *w* for devices with *x* = 0.3 (◇), 0.45 (○), 0.65 (□), and 0.8 (x).

Wide-bandgap (AgCu)(InGa)Se_2 absorber layers with *x* = 0.8 were deposited by the three-stage co-evaporation process under varying Se incident flux and stage-one substrate temperature. Solar cell results are summarized in Figure 16. Increasing Se-to-metals molar flux ratio from Se/M ≈ 5 to Se/M ≈ 20 reduced process variability, but did not result in an overall improvement in device performance. Reducing the substrate temperature during stage-one T_{SS} = 550 to 400ºC also did not affect device performance. Consistent with earlier results, Ag incorporation improved wide bandgap device efficiencies from η ≈ 8% with no Ag to η ≈ 12% with Ag/(Ag+Cu) = 0.75.

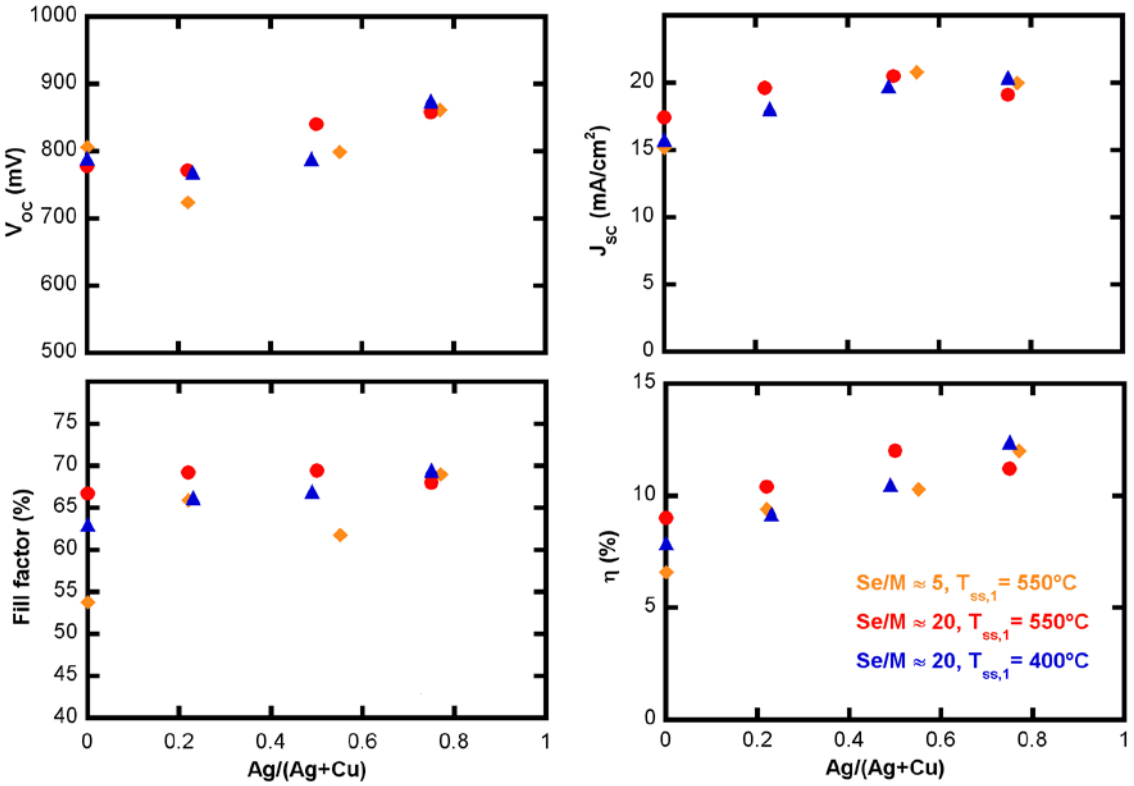

Figure 16. V_{OC}, J_{SC} FF, and efficiency vs. *w* for devices deposited with a three-stage process and varying Se-to-metals and first-stage temperatures.

Finally an MgF_2 anti-reflection layer was deposited on some of the best cells from the studies above. Two notable results are listed in Table VI and their J-V and QE curves are shown in Figure 17. The result with E_g = 1.65 eV is compared to the best reported results with different wide bandgap alloys in Table VII. This result has a higher combination of V_{OC} and efficiency than any of the other alloy cells.

Table VI. J-V parameters for best (AgCu)(InGa)Se_2 cells with low (E_g = 1.3 eV) and high (E_g = 1.65 eV) bandgap, after deposition of an anti-reflection layer.

E_g (eV)	*x*	*w*	Eff (%)	V_{OC} (mV)	J_{SC} (mA/cm^2)	FF (%)	Process
1.3	0.45	0.15	17.6	703	32.2	77.7	Uniform
1.65	0.8	0.76	13.0	890	20.5	71.3	3-stage

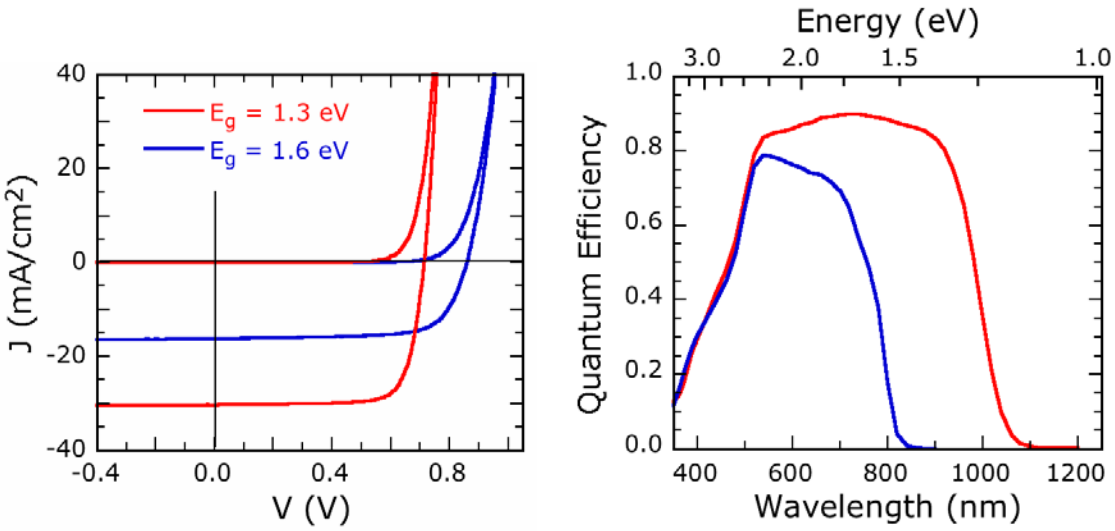

Figure 17. J-V (left) and QE (right) curves of two notable (AgCu)(InGa)Se_2 solar cells.

Table VII. Highest total area efficiencies for wide bandgap devices with different alloy absorber layers.

Material	E_g (eV)	Eff. (%)	V_{OC} (mV)	J_{SC} (mA/cm^2)	FF (%)	Reference
$CuGaSe_2$	1.68	9.5	905	14.9	70.8	[xix]
$Cu(InGa)S_2$	1.53	12.9	832	22.9	67.0	[xx]
$Cu(InAl)Se_2$	1.51	9.9	750	20.1	65.8	[xxi]
$(AgCu)(InGa)Se_2$	1.65	13.0	890	20.5	71.3	[xxii]
$Ag(InGa)Se_2$	1.7	9.3	949	17.0	58	[xxiii]

Diode Analysis

The current–voltage results for the device in Figure 15 were analyzed using the procedure described previously [xxiv] to determine diode parameters including the forward current (J_O), the diode quality factor (A), the series resistance (R_S) and the shunt conductance (G) as defined by the diode equation:

$$J = J_o \; exp\left[\frac{q(V - R_s J)}{AkT}\right] - J_o - J_{sc} + GV \qquad (4)$$

The diode analysis is partly shown in Figure 18 where an (AgCu)(InGa)Se_2 sample with x = 0.3 and w = 0.3 is compared to one with *x* = 0.8 and *w* = 0.2. The light and dark J-V curves are shown at the top. In the middle, the derivative dV/dJ is plotted vs. $(J+J_{SC}-GV)^{-1}$, where G was determined from the minimum slope dJ/dV in reverse bias. The slope on this plot determines A and the intercept determines R_S. Finally, the bottom plot is a semi-logarithmic plot of $(J+J_{SC}-GV)$ vs. $(V-R_SJ)$ where a fit to the linear region at high voltage gives J_O and A. A distinct difference between the samples is seen in the second and third plots. The low Ga cell has similar behavior between the light and dark curves over nearly 2 orders of magnitude in current while with the high Ga device the light data deviates from the dark data and is not exponential. This is

indicative of a voltage-dependent collection of photo-generated current $J_L(V)$ that the above diode analysis does not take into account [xxiv]. As a result, the light J-V data on the high Ga cell cannot be reliably fit to determine the diode parameters under illumination.

QE measurements of the same devices are shown in Figure 19 at two different voltage biases, 0V and -1V. There is negligible difference in the QE curves of the low Ga cell but a significant increase in QE with reverse voltage bias for the high Ga cell. This bias dependence confirms the interpretation of the voltage dependent current collection loss in the J-V data with high Ga. The $J_L(V)$ effect can be quantitatively characterized by calculating the current $J_{QE}(V)$ from the integral over wavelength of the product of the QE and the AM1.5 spectrum and then determining the ratio at different voltage bias. For the devices in this work, this ratio $J_{QE}(-1V) / J_{QE}(0V)$ was determined. All devices with $x \approx 0.3$ and 0.5, except the device with $x = 0.49$ and $w = 0.77$, had values of this ratio in the range 1.00 – 1.02. This indicates that there is little increase in current with the additional field created by the reverse voltage bias. For the devices with $x \approx 0.8$ and the excepted cell with $x = 0.49$ this ratio increases to 1.07 – 1.10 so the added field has a significant effect on improving collection of photo-generated current. Thus, the voltage-dependent collection is observed in all the wide bandgap cells with $E_g > 1.4$ eV, with no apparent difference due to Ag alloying. This leads to a loss in FF and, to a lesser extent, J_{SC}.

One result of the diode analysis is the determination of the diode quality factor which can be an indicator of the recombination that limits device performance. These values, determined by analysis as in Figure 18, are shown in Figure 20. With $x = 0.3$ or 0.5 comparable values of A were obtained from both the dark and light J-V data. These values of A in the range 1.4 ± 0.2 are typical of well-behaved $Cu(InGa)Se_2$ devices. However, with $x = 0.8$, the dark J-V data gave $A \approx 2.0$ while A could not be determined for the light case due to the $J_L(V)$ shown in Figure 18. These J-V characteristics are consistent with V_{OC} controlled by Shockley-Read-Hall (SRH) recombination in the space charge region of the absorber layer [xxv]. A value of $A \approx 2$ is consistent with the trap states for recombination situated nearer to mid-gap in energy [xxvi].

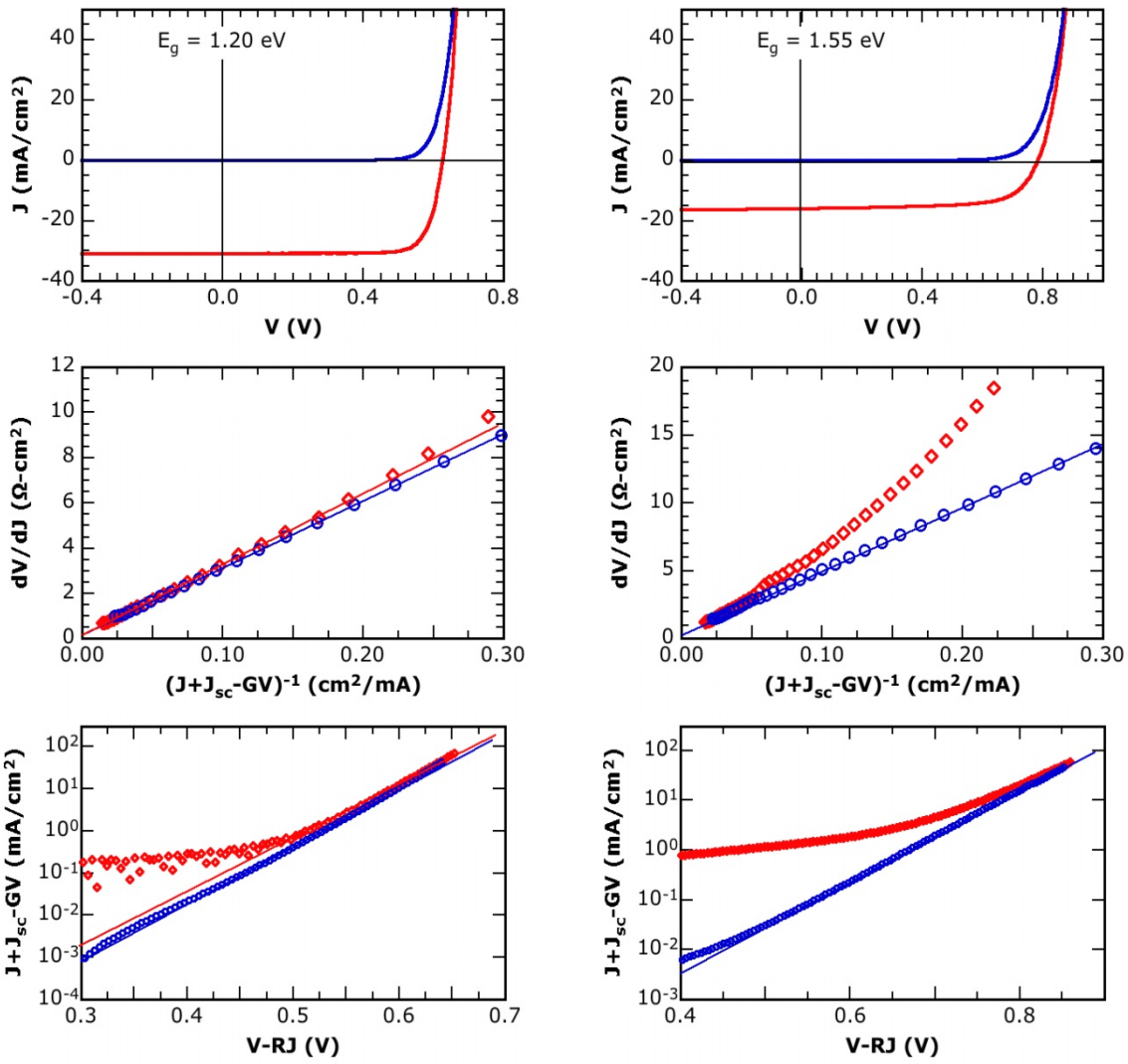

Figure 18. Diode analysis of $(AgCu)(InGa)Se_2$ devices with $x = 0.3$, $w = 0.3$, and $E_g = 1.20$ eV (left) and $E_g = 1.55$ eV, $x = 0.8$ and $w = 0.2$ (right). Data in blue is measured in the dark and data in red under AM1.5 illumination.

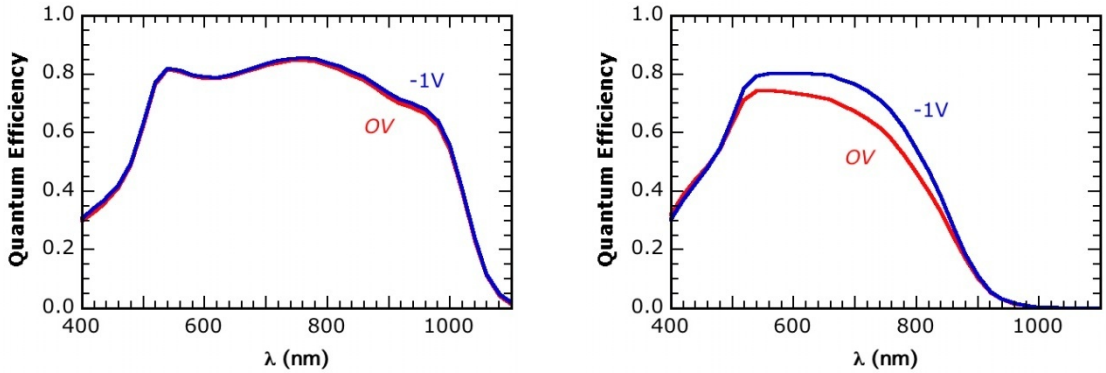

Figure 19. QE measurements under white light bias at 0V (red) and -1V (blue) for the devices in Figure 18.

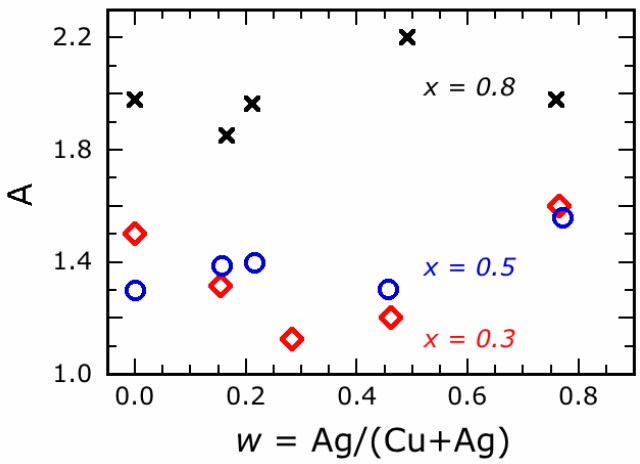

Figure 20. Diode quality factor A for devices in Figure 18.

Sodium Effect

The beneficial role of Na in Cu(InGa)Se_2 has been extensively studied though there is still no conclusive understanding of its role in improving device performance. (AgCu)(InGa)Se_2 films were deposited in a single run with x = 0.46, w = 0.22, and E_g = 1.32 eV on soda lime glass and glass with a Na diffusion barrier. The J-V curves are shown in Figure 21 for the resulting devices. With the reduced Na diffusion V_{OC} decreased by 120 mV and FF decreased from 79 % to 62 %. The decrease in V_{OC} and roll-over behavior are typical of Cu(InGa)Se_2 devices with insufficient Na.

To characterize the mechanism controlling V_{OC} and the decrease with low Na, the temperature dependence of V_{OC} was measured [xxiv,xxvii] as shown in Figure 22. Extrapolation to T = 0K gives the activation energy (E_A) for recombination according to

$$V_{oc} = \frac{E_A}{q} - \frac{AkT}{q} ln\left(\frac{J_{oo}}{J_L}\right) \qquad (5)$$

which follows from Eq. 1 with an Arrhenius behavior for the forward current J_O. The cell on a SLG substrate has $E_A = E_g$ which indicates that the dominant recombination occurs in the absorber layer and is again consistent with SRH recombination in the (AgCu)(InGa)Se_2 space charge region. Two differences are seen with the Na barrier substrate. First is a lower E_A which has been attributed to interface recombination limiting V_{OC} [xxvii]. Second is a saturation of V_{OC} as temperature decreases which indicates a freezing out of the recombination.

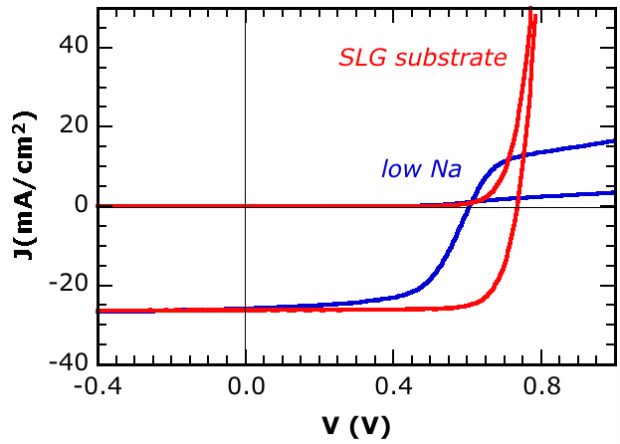

Figure 21. J-V curves in the dark and under AM1.5 illumination for devices on soda lime glass and on glass with a Na diffusion barrier.

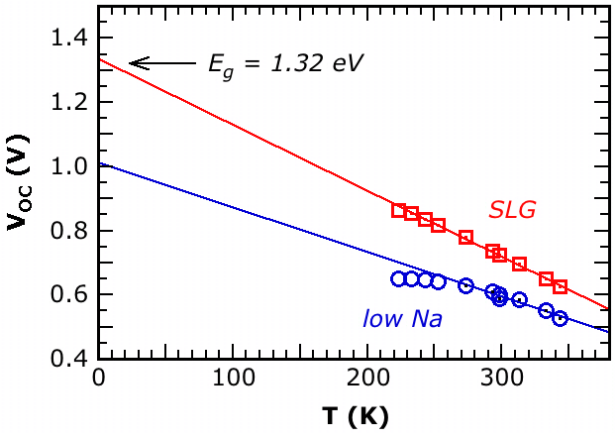

Figure 22. The temperature dependence of V_{OC} for the devices with E_g = 1.32 eV in Figure 21 and extrapolation to T=0 to determine E_A.

VI Characterization of electronic properties

The measurements employed in our characterization of the electronic properties of the (AgCu)(InGa)Se_2 absorbers utilize a set of experimental techniques which have all been described previously in some detail. They consist of (1) admittance spectroscopy as a function of temperature and frequency, (2) drive-level capacitance profiling, and (3) transient photocapacitance. Below we describe each method only very briefly, and then present some examples on the (AgCu)(InGa)Se_2 samples we have studied. Finally we summarize the information obtained on these (AgCu)(InGa)Se_2 samples and formulate some general conclusions.

Admittance spectroscopy

These working (AgCu)(InGa)Se_2 heterojunction cells contain a depletion region which is first characterized by recording the ac admittance as a function of temperature and frequency. This is

done prior to carrying out the DLCP and transient photocapacitance measurements described below. The capacitance phase of these measurements often exhibit a distinct step and an Arrhenius plot of this step over a range of frequencies and measurement temperatures provides us with an activation energy, E_a, which we attribute to the energetic position of a deep acceptor defect, E_D, relative to the valence band: $E_a = E_D - E_V$. For these (AgCu)(InGa)Se_2 samples such a distinct step often only appears after these samples have been exposed to light exposure to above bandgap illumination, as illustrated in Figure 23. These admittance measurements also give us an indication of the quality of the barrier junction, information that allows us to pre-screen the sample devices for further measurements using our more advanced methods.

Drive-level capacitance profiling

The drive-level capacitance profiling method has been described in detail in previous publications [xxviii,xxix]. It is similar to other kinds of capacitance profiling in that it provides us with a density *vs*. distance profile; however, this particular method was developed specifically to address the difficulties encountered in interpreting capacitance measurements in materials with defect densities comparable to carrier densities. In this method we monitor the junction capacitance both as a function of DC bias, V_B, and as a function of the amplitude of the alternating exciting voltage, δV. To lowest order this dependence has the form: $C(V_B,\delta V) = C_0(V_B) + C_1(V_B)\,\delta V + \ldots$, and that the ratio:

$$N_{DL} \equiv \frac{C_0^3}{2q_e \varepsilon A^2 C_1} = p + \int_{E_F^o}^{E_V + E_e} g(E)dE \qquad (6)$$

is directly related to the free carrier density, p, plus an integral over the gap states as indicated. Here E_F^o is the bulk Fermi level position in the sample and E_e depends on the frequency, ω, and temperature of measurement: $E_e(\omega,T) = k_B T \log(\nu/\omega)$. Thus, by altering the measurement temperature (or frequency) we obtain information about the energy distribution of the defects. By altering the applied DC bias, we can vary the spatial region at which we detect the defects in the sample and thus can spatially profile the defects as a function of the position from the barrier interface. Examples of DLCP profiles for one (AgCu)(InGa)Se_2 samples both above and below the admittance step in two partially light soaked states are shown in Figure 24.

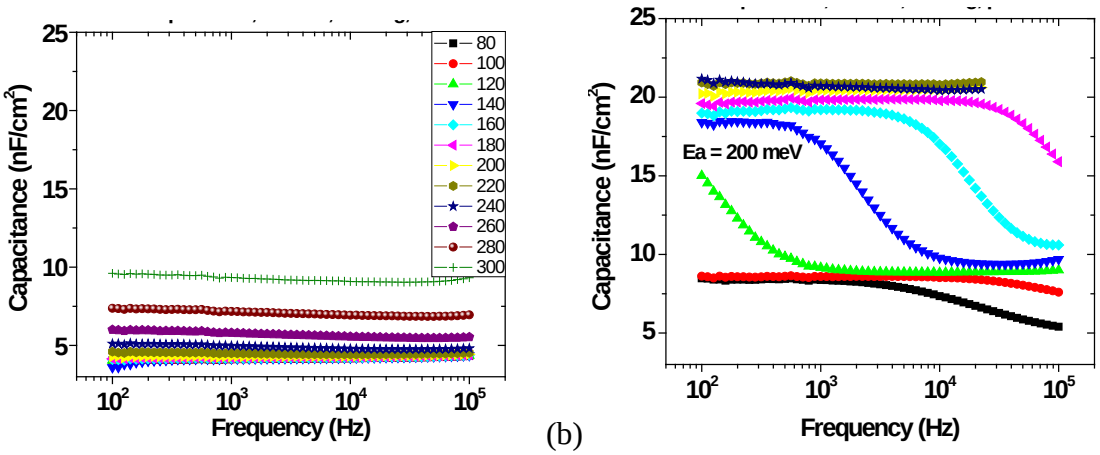

Figure 23. Typical admittance spectra for an (AgCu)(InGa)Se_2 sample (34235 with a 28% Ag and a 30% Ga fraction). (a) While there is no apparent defect features in the fully annealed state, (b) a very evident activated step (E_a = 200meV) appears after the sample has been light soaked with AM1.5 light for two hours. This step begins to anneal away at 250 K, much like a similar feature in Cu(InGa)Se_2 without Ag, and returns to its initial state after a 20 minute anneal in the dark at 320K.

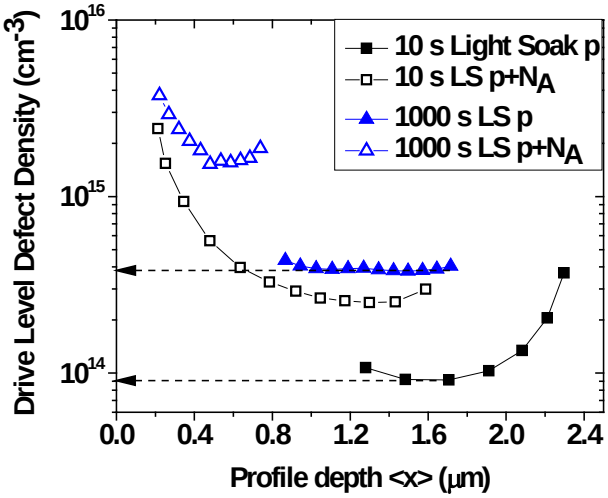

Figure 24. 10kHz DLCP profiles for (AgCu)(InGa)Se_2 sample 34244 (having Ag and Ga fractions near 50%) are shown for temperatures both above and below the admittance step for two metastable states produced by AM1.5 light soaking for 10s and 1000s at 250K. The solid symbols (for a temperature below the step) reveal the carrier concentrations while the open symbols (taken above the step) reveal the *sum* of the carrier plus deep acceptor densities. In the fully annealed state of this sample the DLCP profiles indicated very low free carrier and deep acceptor densities (near 10^{14} cm^{-3}).

Transient photocapacitance spectroscopy

The method of junction transient photocapacitance (TPC) spectroscopy has been discussed in great detail over the years in the literature [xxx,xxxi,xxxii]. It represents a type of sub-band-gap optical spectroscopy and provide spectra quite similar in appearance to a sub-band-gap optical

absorption spectra. However, instead of detecting absorbed energy, the TPC method detects the optically induced change in defect charge within the depletion region.

In this method the space charge region of the semiconductor near the barrier junction is first subjected to a voltage "filling pulse". This pulse causes the deep defect states in the gap to be filled with holes. As time progresses, the initial steady-state population is recovered through the excitation of these trapped holes to the valence band where they then move out of the depletion region under the influence of the electric field. In the dark this proceeds entirely by the thermal excitation of trapped carriers. However, this process can be enhanced through optical excitation and this is the basis of the TPC method.

In the actual measurements, the sub-band-gap light is applied after *every other* filling pulse so that the capacitance transients with and without light present can be subtracted. The capacitance transient signals are then integrated over a "time window"-- between t_1 and t_2 --following each filling pulse, and the *difference* is obtained for sequential pairs of transients, with and without light present. When this difference is normalized to the photon flux it yields the *photocapacitance signal*, S_{TPC}, at the photon energy, E_{opt}, selected by the monochromator. Specifically:

$$S_{TPC}(E_{opt}) \equiv \frac{\int_{t_1}^{t_2} C_{light}(t)dt - \int_{t_1}^{t_2} C_{dark}(t)dt}{Photon\ Flux\ at\ E_{opt}} \qquad (7)$$

Repeating this over the full range of sub-bandgap photon energies available yields the *photocapacitance spectrum*. In such measurements it is important to work in the linear regime (low enough light levels) such that S_{TPC} will be independent of the intensity of light used. Examples of such photocapacitance spectra for (AgCu)(InGa)Se_2 sample devices are shown in Figures 25, 26, and 27.

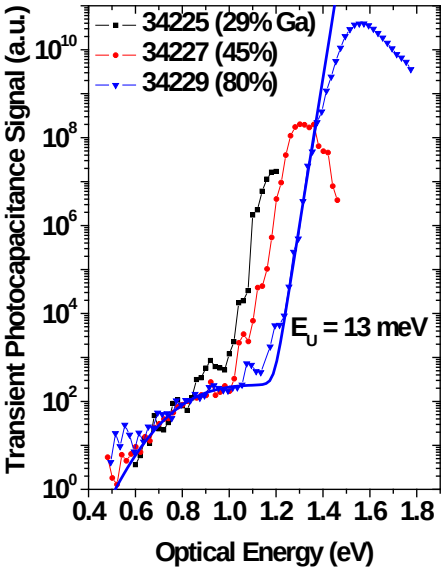

Figure 25. Transient photocapacitance spectra of three 16% Ag fraction (AgCu)(InGa)Se_2 samples with varying amounts of Ga. The blue line through the 80% Ga fraction sample is a fit assuming that the optical transitions comprise an exponential bandtail plus a Gaussian deep defect distribution. The characteristic slopes of the exponential band tail (Urbach energy) were determined to be 15, 14, and 13 meV in order of increasing Ga fraction, significantly lower than those in corresponding Cu(InGa)Se_2 samples without Ag. (See Figure 27) The sub band gap defect signal (shoulder feature) can be fit with a defect centered near 0.8 eV in all of these spectra, similar to the defect signal found in Cu(InGa)Se_2.[xxxiii]

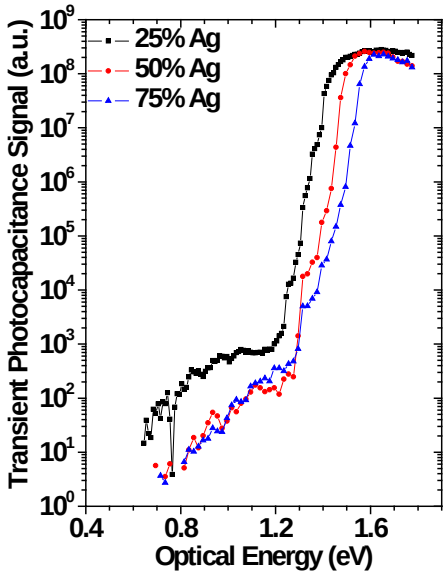

Figure 26. TPC spectra for (AgCu)(InGa)Se_2 with 80% Ga and varying Ag fractions. The spectra show the increasing band gap with increasing silver fraction. They also indicate a modified energy distribution for the deep defect at higher Ag.

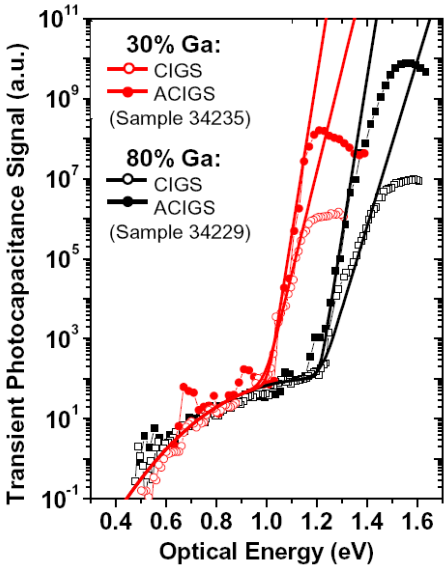

Figure 27. Devices incorporating Ag into the Cu(InGa)Se_2 chalcopyrite lattice have steeper Urbach edges than those without Ag. All of the sub-band gap defect (shoulder) features have been fit with the same Gaussian distribution centered at 0.8eV.

The kind of information obtained by such TPC spectra is illustrated in Figure 25, which compares 3 spectra for (AgCu)(InGa)Se_2 samples all having Ag fractions of 16% but with varying Ga fractions. All these spectra exhibit an exponentially increasing signal with optical energy 0.15 to 0.25eV below the bandgap energy (the "bandtail" regime) as well as a shoulder of transitions extending below this to an optical transition energy of 0.5eV (the "deep defect" regime). We have aligned the TPC spectra for this set of samples to overlap in the deep defect regime to illustrate that the energy distributions of these transitions are nearly identical, and are well fit by a Gaussian band of transitions centered near 0.8eV. The bandtail regime is characterized by its exponential slope or "Urbach energy", E_U. For the highest Ga fraction sample we show the detailed fit of the TPC spectrum which indicates a value for E_U in that case of 13meV. The values of E_U for the other two samples are very similar.

In Figure 26 we display the TPC spectra for 3 samples containing 80% Ga fractions but with varying Ag fractions. These spectra clearly show how the (AgCu)(InGa)Se_2 bandgap increases with increasing Ag fraction. Table I indicates that among the five (AgCu)(InGa)Se_2 samples studied with 80% Ga fractions, the two samples with Ag fractions near 25% had significantly larger bandtail widths (i.e., higher values of E_U). This indicates an increased level of disorder for this composition range, and is possibly related to findings from a previous study that single phase (AgCu)(InGa)Se_2 alloys in this composition range were impossible to obtain from the melt.[xxxiv]

Figure 27 provides a comparison of two pairs of Cu(InGa)Se_2 alloys with and without Ag but the same Ga fractions (30% and 80%). The bandtails are clearly much steeper in the (AgCu)(InGa)Se_2 samples. Indeed, most of the (AgCu)(InGa)Se_2 samples examined using TPC exhibited Urbach energies below 15mev (see Table VIII) while, in comparison, values of E_U for the Cu(InGa)Se_2 alloys without Ag generally lie between 18 and 25meV.[xxxii] We hypothesize

that this apparent decrease in the structural disorder in the (AgCu)(InGa)Se_2 alloys results from their lower melting points.

Summary and relationship of results to device performance

Table VIII summarizes the information obtained by our DLCP and TPC measurements for the 12 samples fully characterized by these methods. The cell performance parameters are also listed. In all cases the information displayed corresponds to the "annealed state" (325K for 10 minutes in the dark). Although light exposure affects some of the deduced quantities such as the free carrier and deep acceptor densities, such light induced effects are largely reversed after several hours in the dark at room temperature.

Previous studies of Cu(InGa)Se_2 sample devices of similar bandgaps have suggested that higher values of E_U were correlated with lower values of J_{SC} [xxxii]. In studies of Cu(InGa)Se_2 alloyed with sulfur we also found a deleterious effect for larger values of E_U on the "V_{OC} deficit"; i.e., the difference between the bandgap and open-circuit voltage.[xxxv] However, these effects only appeared for values of E_U in excess of roughly 20meV and thus, not surprisingly, do not seem to be correlated with either J_{SC} or V_{OC} for the current set of devices. Perhaps more relevant to the device performance of these samples may be the very low carrier densities deduced by DLCP which are close to 10^{14} cm^{-3}, rather than 10^{15} cm^{-3} or higher values that have been reported for most Cu(InGa)Se_2 absorbers fabricated at IEC.[xxix] performance of these samples may be the very low carrier densities deduced by DLCP which are close to 10^{14} cm^{-3}, rather than 10^{15} cm^{-3} or higher values that have been reported for most Cu(InGa)Se_2 absorbers fabricated at IEC.[xxix]

One interesting special case is sample 34232 which had a much larger voltage deficit than any of the other (AgCu)(InGa)Se_2 samples examined. This sample alone exhibited an unusual TPC spectrum [see Figure 28] indicating that the absorber was not single phase but contained a small admixture of a second phase, likely $AgInSe_2$ (on the basis of its optical threshold). However, the volume fraction of this phase was estimated to be no more than 0.01% and thus too small to be revealed by X-ray diffraction. The TPC spectrum for a second sample subsequently fabricated with the same Ag and Ga fractions (34337) did not exhibit any evidence for such multiple phases, although its relatively high value of E_U does indicate a higher level of disorder than the other (AgCu)(InGa)Se_2 samples. In any event, the results from these two samples demonstrate the extreme sensitivity of our experimental methods to subtle variations in the electronic properties of the absorber that can clearly significantly impact solar cell performance.

Table VIII. (AgCu)(InGa)Se_2 devices characterized, grouped by Ag content. Performance parameters are listed along with free carrier and deep acceptor densities determined by DLCP, and Urbach energies from TPC. Values listed were obtained for the annealed state of each sample.

Sample	*w*	*x*	E_g (eV)	V_{OC} (V)	J_{SC} (mA/cm^2)	FF (%)	Eff (%)	p (10^{14} cm^{-3})	N_A (10^{14} cm^{-3})	E_U (meV)
34225	0.16	0.29	1.20	0.63	32.8	77.3	16.0	4.0	>8.0	15
34227	0.16	0.45	1.30	0.70	30.0	76.4	16.1	1.0	>3.0	14
34228	0.15	0.56	1.38	0.73	25.6	68.9	12.8	1.2	>9.0	17
34229	0.16	0.80	1.54	0.76	17.7	65.8	8.8	1.8	>9.0	13

34235	0.28	0.30	1.22	0.63	30.7	76.1	14.7	1.0	~ 1.0	10
34234	0.28	0.47	1.33	0.58	25.8	58.5	8.8	1.0	2.0	13
34337	0.25	0.80	1.55	0.79	15.1	63.6	7.6	2.0	4.0	18
34232	0.27	0.81	1.56	0.63	18.7	61.5	7.3	1.1	1.9	20
34244	0.46	0.50	1.36	0.75	24.4	72	13.1	0.6	1.2	11
34276	0.50	0.83	1.60	0.79	15.9	53	6.5	1.0	3.8	12
34254	0.76	0.53	1.48	0.77	22.4	69	11.8	0.7	2.3	12
34259	0.76	0.81	1.65	0.84	16.3	66	9.1	1.0	5.0	15

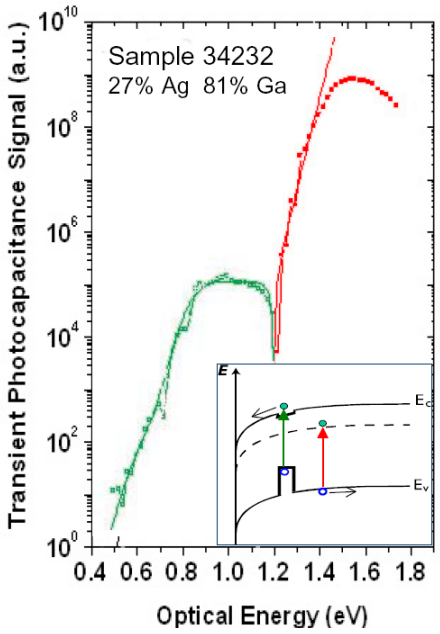

Figure 28. Unusual photocapacitance spectra for one (AgCu)(InGa)Se_2 sample showing a region of *negative* TPC signals (green portion) for optical energies below 1.24eV. This indicates a transition of the type shown in the inset diagram involving the optically induced release of an electron instead of a hole from the depletion region. The 1.24eV threshold suggests that this negative signal may originate from small inclusions of $AgInSe_2$ within the absorber as also schematically indicated in the inset diagram. However, the magnitude of the negative signal compared to the *positive* TPC signal magnitude at 1.5eV indicates that the hypothesized $AgInSe_2$ phase would account for less than 0.01% of the total volume fraction of the absorber.

VII. Post Deposition Annealing

Pulsed Laser Annealing

$Cu(InGa)Se_2$ and $(AgCu)(InGa)Se_2$ films have been treated using pulsed laser annealing to determine if the defect structure and electronic properties of the films can be modified to improve device performance. The annealed films have been characterized by SEM, EDS, and XRD and the electronic properties were characterized by the device properties.

This work utilized a commercial Nd:YAG laser micro-machining system (Model 5024, U.S. Laser Corporation) which is also used for laser scribing for monolithic integration of thin film PV modules. Since laser annealing requires much less beam energy density than laser scribing, it was deemed critical to understand the manipulation parameters and their control ranges, and ultimately determine whether this system could be successfully utilized for laser/film interaction studies.

The schematic diagram of the laser system is shown in Figure 29. The laser beam with a 532 nm wavelength, ~ 600 μm waist diameter and 6 ns pulse width generates a wide range of beam power (0.04 ~ 3.1 W) depending on the current (14 ~ 27A) and repetition rate (1 ~ 35 kHz). The short wavelength is used so that there is very high absorption in the $Cu(InGa)Se_2$ (>95% in the top 0.3 μm) and modification can be confined to the near surface. Additional reduction of the beam power can be achieved by a power attenuator composed of a fixed polarizer and a rotatable wave plate. Furthermore, the variable feed rate of the X-Y table (0.127 ~ 152 mm/s) allows more flexibility in actual beam density exposed to the sample. In this system, the beam size of the laser is adjusted by a built-in upcollimator (2 ~ 8×) and external beam expander (1 ~ 10×) which can be inserted between the dichroic mirror and upcollimator. Intentional defocusing of the beam or removal of the objective lens from the focusing barrel, as illustrated in Figure 29, can also change both the beam size and intensity.

A broad range of surface modifications that can be obtained by changing focal conditions is shown in Figures 30 - 32 on $Cu(InGa)Se_2$ films with 2 μm thickness and [Ga]/[In+Ga] = 0.3, which were deposited on Mo-coated soda lime glass by co-evaporation. Half of each 1″×1″ $Cu(InGa)Se_2$ sample was laser annealed under atmospheric air ambient to enable controlled characterization. Low beam power (14 A / 20 kHz ~ 70 mW) was applied for these annealing experiments. The beam diameter was estimated using a laser burn paper and SEM analysis, and 10% of the beam diameter was set as a hatch spacing (i.e., beam overlap size). The feed rate of the X-Y table was fixed at 150 mm/s. The annealed surface looks uniform in SEM micrographs despite multiple scans with a relatively small beam diameter (30~100 μm), which supports the expandability of this technique to large scale.

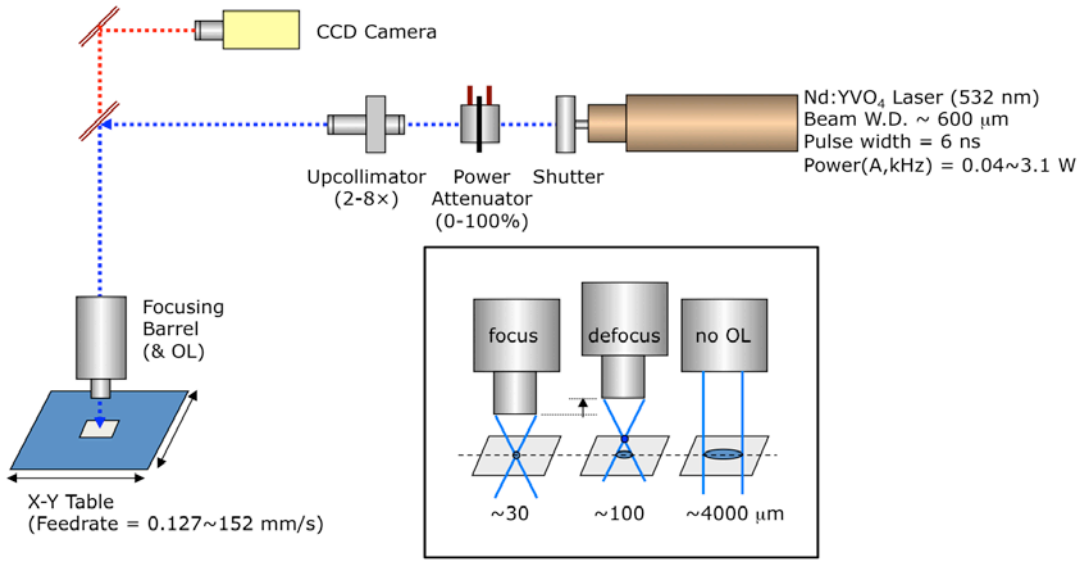

Figure 29. Schematic diagram of the laser processing system at IEC. The inset shows the range of options for the objective lens (OL) and focusing barrel.

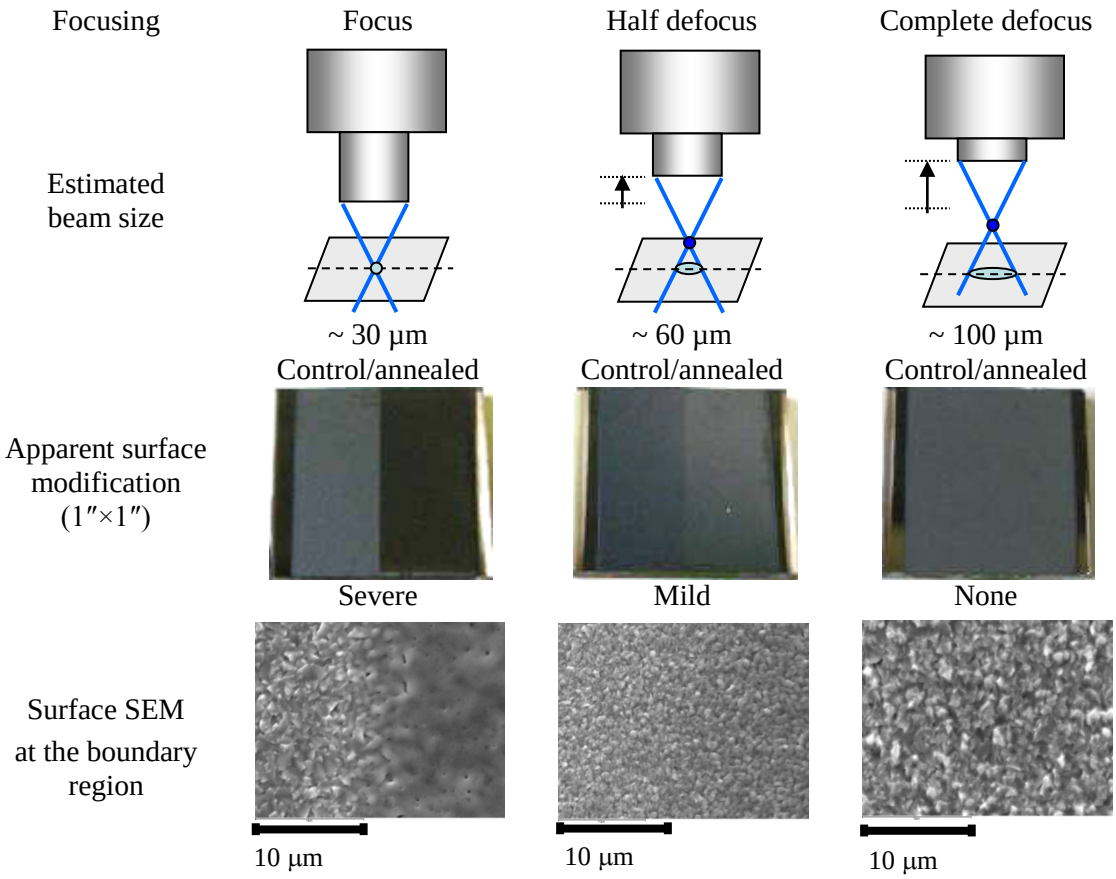

Figure 30. Laser annealing results of $Cu(InGa)Se_2$ films at different focusing conditions.

The degree of surface modifications by these laser conditions are listed as severe, mild and none. For the sample with "severe" surface modification, surface and cross-sectional SEM images are shown in Figure 31. The SEM surface image suggests that the beam intensity was strong enough to melt the surface. No apparent change is observed in the bulk structure from the cross-sectional SEM images consistent with absorption of the optical energy in the near surface region. No measurable change in the composition of the annealed films in Figure 30 could be discerned by EDS.

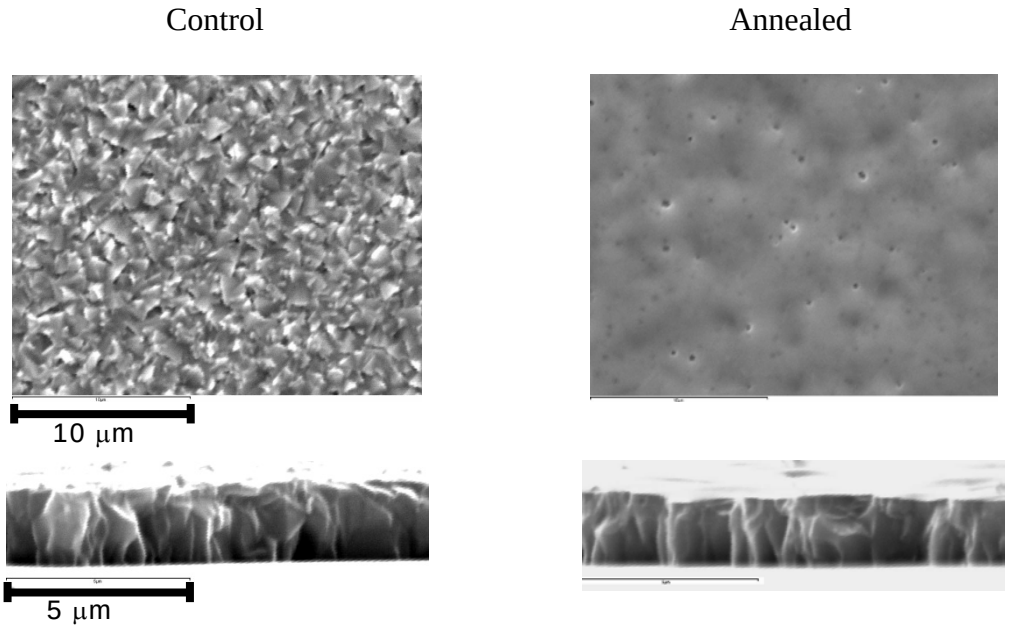

Figure 31. Surface and cross-sectional SEM images of laser annealed $Cu(InGa)Se_2$.

XRD spectra of the three annealed samples are compared with the corresponding control samples in Figure 32. Partial recrystallization of the $Cu(InGa)Se_2$ is indicated for the films with severe and mild surface modifications, evidenced by the relative increase of the intensity in (112) peak relative to (220/204) and (312/116) peaks.

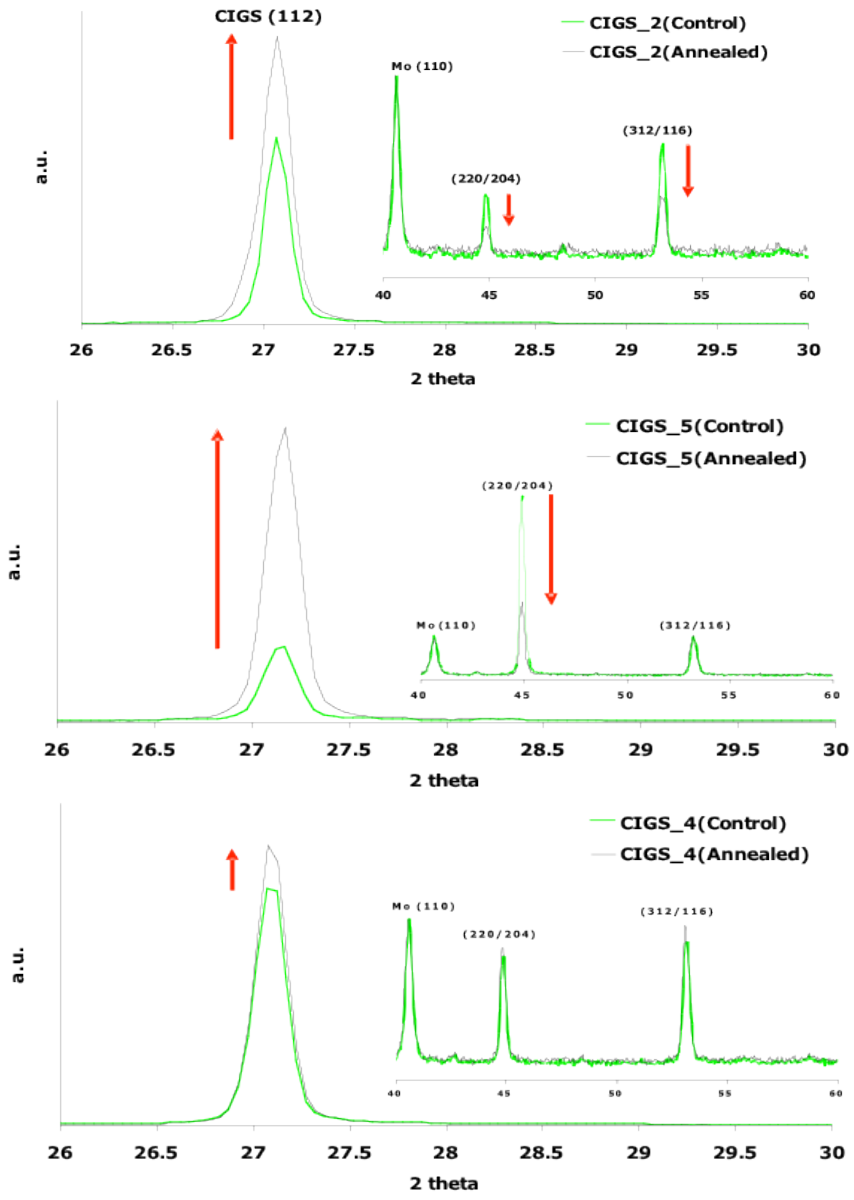

Figure 32. XRD results of Cu(InGa)Se_2 absorbers laser annealed to create severe (top), mild (middle), and no change in surface morphology. Peak intensities were normalized by the Mo(110) intensity.

Solar cells were fabricated using a wide range of anneal conditions including those that resulted in the surface and structural changes above. It was found that any of the film modifications shown lead to reduced device performance and generally shunted solar cells. Better results were obtained by annealing at lower energy densities using a laser beam with the objective lens removed from the focusing barrel to create, an enlarged beam diameter (~4000 μm). To compensate for the attenuation of the laser energy density due to the magnified beam size, the motion of the X-Y sample table was programmed for a relatively slow feed rate (0.5 mm/s) and large hatch space (50~88%) increasing laser exposure time per unit area. A maximum laser power (3.1W at 27A/35kHz) was employed. With these anneal conditions, XRD, GIXRD, SEM

and EDS characterization showed no changes in crystal structure, orientation or composition. J-V curves and parameters, shown in Figure 33 and Table IX for a sample with a co-evaporated $Cu(InGa)Se_2$ absorber with 2 μm thickness and [Ga]/[In+Ga] = 0.55, gave improved device performance relative to the unannealed control samples on the same substrate. The difference is due to higher FF as a result of improved current collection, as c0nfirmed by bias –dependent QE measurements (not shown).

Table IX Summary of device results for laser annealing with Power = 3.1 W, beam size = 4000 μm, feed rate = 0.5 mm/s and different hatch spacing.

Sample	Device	Voc (V)	Jsc (mA/cm^2)	Ff (%)	eff (%)
34242.33	annealed	0.72	21.9	68.2	10.7
	control	0.72	18.0	57.1	7.5

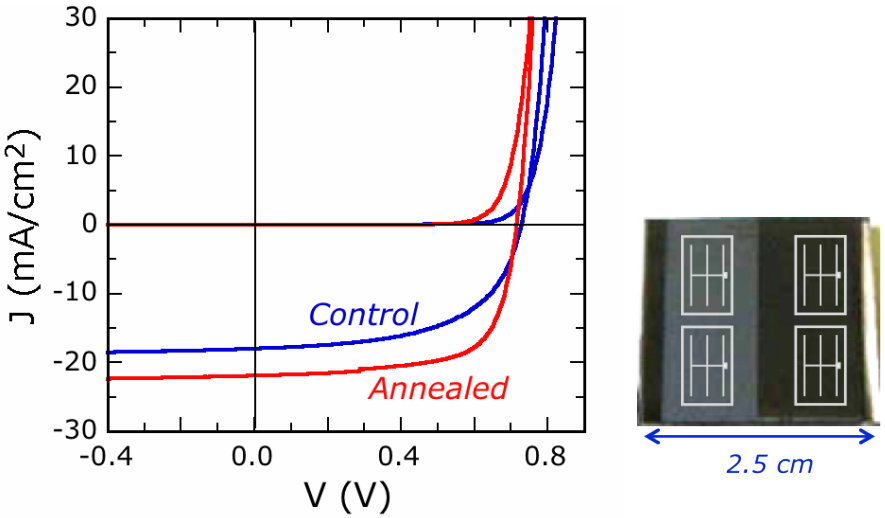

Figure 33. J-V curves for devices in Table IX. The picture on right illustrates how control and annealed devices are configured on a single 1" x 1" substrate.

In addition to annealing the exposed $Cu(InGa)Se_2$ surface, a procedure was developed for Se capping the films to protect them during subsequent laser annealing. This was intended to provide excess Se at the surface which might reduce the concentration of point defects related to Se vacancies. $Cu(InGa)Se_2$/Se samples were prepared by depositing Se onto the as-grown $Cu(InGa)Se_2$ layer with no intentional heating of substrate in the evaporation system and no air exposure of the films between layers. Se layers with thicknesses of 100 or 300 nm were used.

The Se layers contributed no peaks to XRD scans of the $Cu(InGa)Se_2$ /Se bilayers so it was assumed that the as-deposited Se was amorphous. The laser treatments generally crystallized the Se layers and comparison of EDS results between control and laser-annealed areas of $Cu(InGa)Se_2$/Se films suggested that there was no significant Se loss during laser annealing. The annealing was done with a range of focus and scan parameters and at laser wavelengths of 532 or 1064 nm to improve transmission through Se layer because the absorbance of Se at 532 nm wavelength is about 30 times higher than at 1064 nm wavelength. After laser annealing of the

bilayer Cu(InGa)Se_2/Se samples, the Se layer was selectively removed by a 0.5 M KCN etch (1.5 m at 60°C)..

Characterization of the films by XRD, EDS, and XPS showed no measurable differences in the structure or composition due to the annealing. Devices with different annealing conditions and different Se capping layers all had no change or reduced efficiency and, in particular, no conditions were found that increased V_{OC}. This was repeated with both low and high bandgap Cu(InGa)Se_2 films.

Thermal Annealing

A second approach to post-deposition annealing using a rapid thermal annealing (RTA) process was also investigated as a means to improve electronic properties of wide bandgap absorber layers. A reactor for of the annealing was designed and built for annealing films at temperatures up to ~ 600°C and for short times before the glass overheats and deforms. A schematic diagram is shown in Figure 34 and a photograph in Figure 35. Samples sit film-side up on a graphite holder inside a quartz tube with radiation from a halogen lamp illuminating the sample through both the quartz tube and a quartz cover plate. Thermocouples (TC's) are embedded into the quartz cover plate and graphite holder. The tube can be evacuated and back-filled with different gases, to modify the reaction atmosphere.

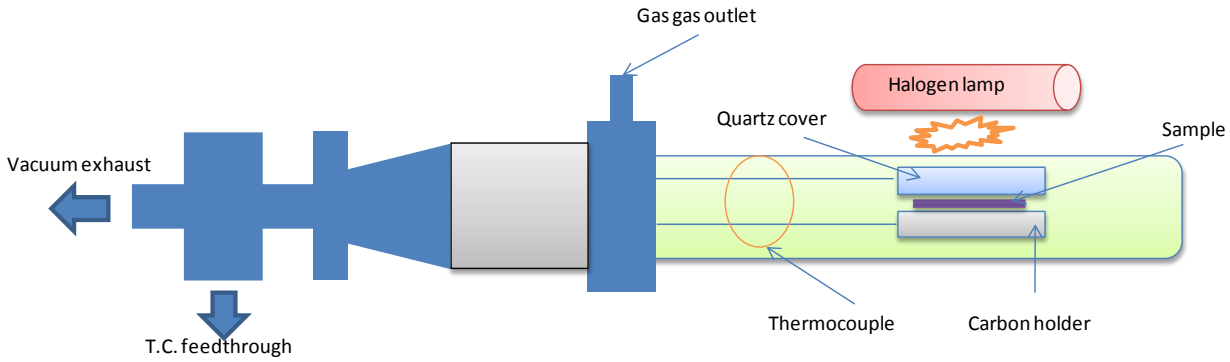

Figure 34. Schematic diagram of the RTA system

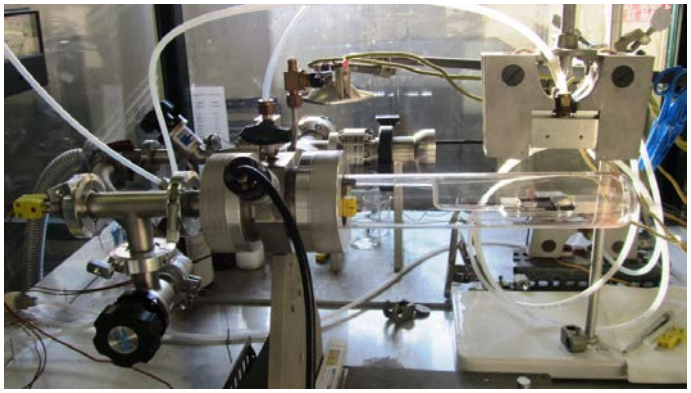

Figure 35. Photograph of the IEC RTA system

Temperature calibrations were performed using an additional TC attached to the surface of a standard glass/Mo/Cu(InGa)Se_2 sample. Figure 36 shows time-temperature profiles using this TC under 40% output lamp power. The profile was measured twice and the profiles were nearly identical. Within 25 s, the surface temperature is over 585°C and then increases more slowly to get to 600°C at 30 s. The sample surface temperature as a function of the output power is also shown. Each temperature was measured at 30 s. However, with > 45 % output power, the surface temperature begins to saturate and is irreproducible. Thus, subsequent experiments were done with 40% power and different set point temperatures.

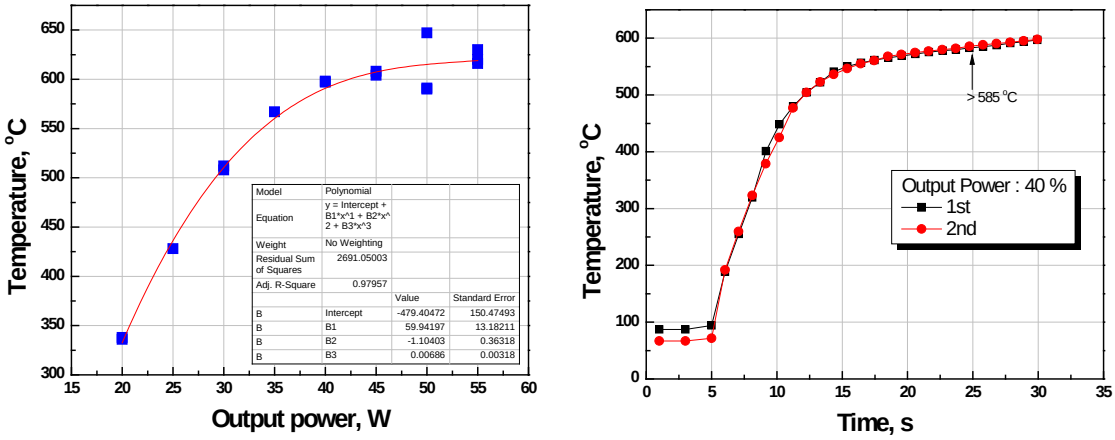

Figure 36. Sample surface temperature vs. lamp power calibration (left) and time - temperature profiles measured under 40% output power condition for the RTA reactor.

RTA experiments have been done on wide bandgap Cu(InGa)Se_2 films with x = 0.8 and (AgCu)(InGa)Se_2 films with x = 0.8 and w = 0.75. All films were deposited using a single layer co-evaporation process and with standard 2.0 µm thickness. A range of annealing conditions were explored including variation of the set point temperature measured on the quartz cover glass from 400 to 600°C, times from 40 to 100 s (including ~30 s ramp-up time), and ambient inside the tube of either Ar or Ar+4%H_2. Times > 100 s or temperatures ≥ 580°C caused warping of the glass or delamination of the films.

In addition to annealing under Ar or forming gas, annealing experiments were done with excess Se to potentially reduce the concentration of Se vacancies that might contribute to recombination. The excess Se was incorporated from a 200 nm thick Se layer deposited either on the surface of the Cu(InGa)Se_2 or (AgCu)(InGa)Se_2 films or on the quartz cover plate. After annealing, the samples were etched in KCN to remove any residual Se layer.

The effect of the RTA treatments on solar cell performance are shown in Figure 37 for four cases. The films were annealed at temperatures from 400 to 575°C with a ramp time of 20 s, dwell time of 30 s at the specified temperature and cooling time of ≤ 10 s to reach 300°C. The cases include Cu(InGa)Se_2 annealed in Ar and (AgCu)(InGa)Se_2 annealed in Ar and with excess Se provided from layers on the quartz and on the sample surface. In each case, the best efficiency and V_{OC} were achieved with anneals at 500°C. Higher temperatures resulted in lower V_{OC} and typically lower FF. J-V parameters for the four cases shown after the 500°C anneals are listed in

Table X. The best efficiency and V_{OC} were achieved using the Se cap deposited directly on the film. The Se on the quartz plate may have evaporated and escaped before the anneal was completed. While the best cells in this study did not exceed the performance of the best cells reported earlier, the results suggest that RTA treatments on wide bandgap (AgCu)(InGa)Se_2 films can improve the subsequent solar cells and that there may be some benefit to the Se capping.

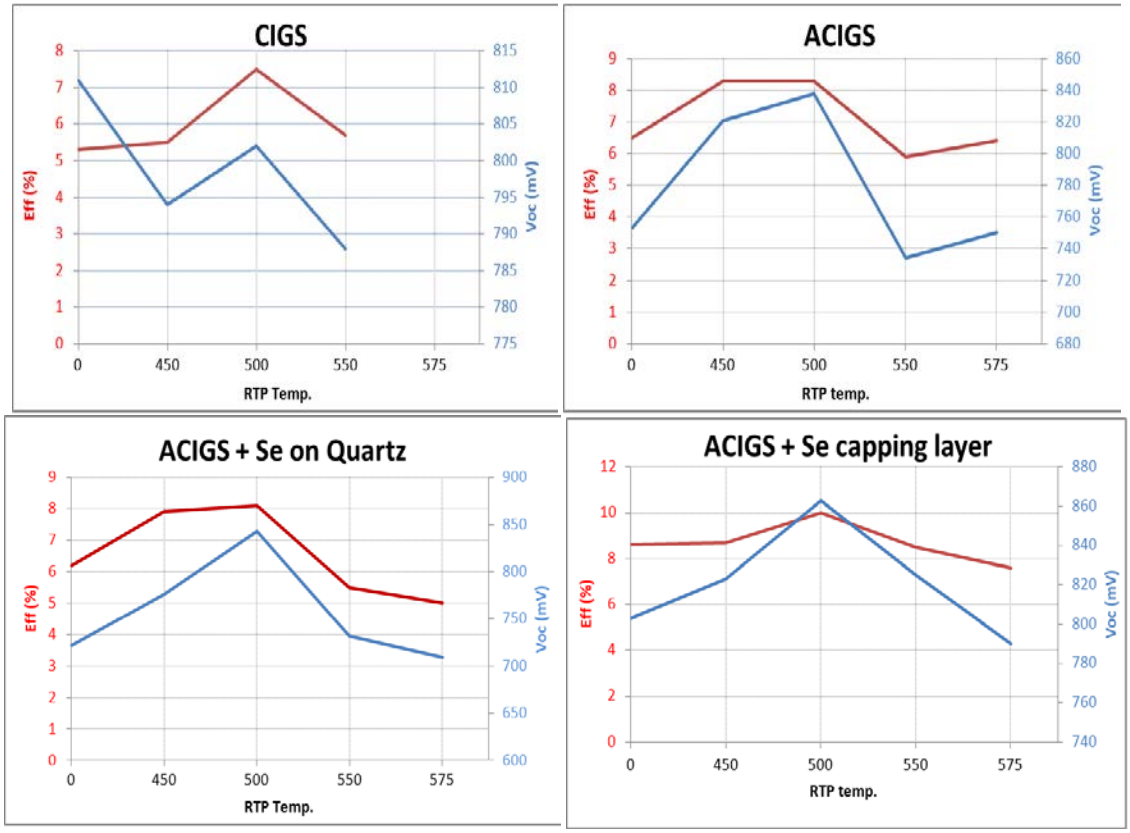

Figure 37. Device efficiency and V_{OC} for Cu(InGa)Se_2 films with x = 0.8 annealed in Ar and (AgCu)(InGa)Se_2 films with x = 0.8 and w = 0.75 annealed in Ar and with Se caps on the quartz cover plate and on the film.

Table X. J-V parameters of the (AgCu)(InGa)Se_2 films annealed in Ar and with extra Se layers.

Sample	T_{RTA} (C)	V_{OC} (mV)	J_{SC} (mA/cm^2)	FF (%)	Eff. (%)
(AgCu)(InGa)Se_2	Ref	753	17.1	50.9	6.5
(AgCu)(InGa)Se_2	500	838	17.0	58.7	8.3
(AgCu)(InGa)Se_2 + Se on quartz	500	843	15.3	63.2	8.1
(AgCu)(InGa)Se_2 + Se capping	500	863	18.1	64.7	10.0

Other RTA treatments using the range of annealing parameters described above including different times, temperatures, and the use of forming gas, did not show any improvement in device performance.

Characterization of $Cu(InGa)Se_2$ and $(AgCu)(InGa)Se_2$ films after the RTA experiments revealed no changes could in bulk properties of the films. This includes modifications to morphology (SEM), composition (EDS), or structure (XRD). Since the RTA processes are intended to modify the near-surface of the films without overheating the bulk film, additional surface characterization was done by glancing incidence GIXRD and XPS.

GIXRD measurements were done with 0.5° incident angle to give a sampling depth of 110 nm. While no significant change was observed with $Cu(InGa)Se_2$ films, there was a change to the surface observed with $(AgCu)(InGa)Se_2$ as shown in Figure 38. The unannealed control samples have an unidentified secondary peak at 27.6° which is not seen in a standard θ-2θ XRD scan indicating an unknown surface phase. As shown, however, RTA treatment at 500°C decreased the unknown peak and completely eliminated it when performed with excess Se. A wider range of samples were characterized with the GIXRD and the unidentified peak was consistently observed in the composition range [Ag]/[Ag+Cu] > 0.5 and 0.5 < [Ga]/[In+Ga] < 0.8. Furthermore, the peak position of the unknown phase remained invariant from the [Ag]/[Ag+Cu] ratio but it moved to a higher angle with increasing [Cu]/[In+Ga] ratio (not shown here).

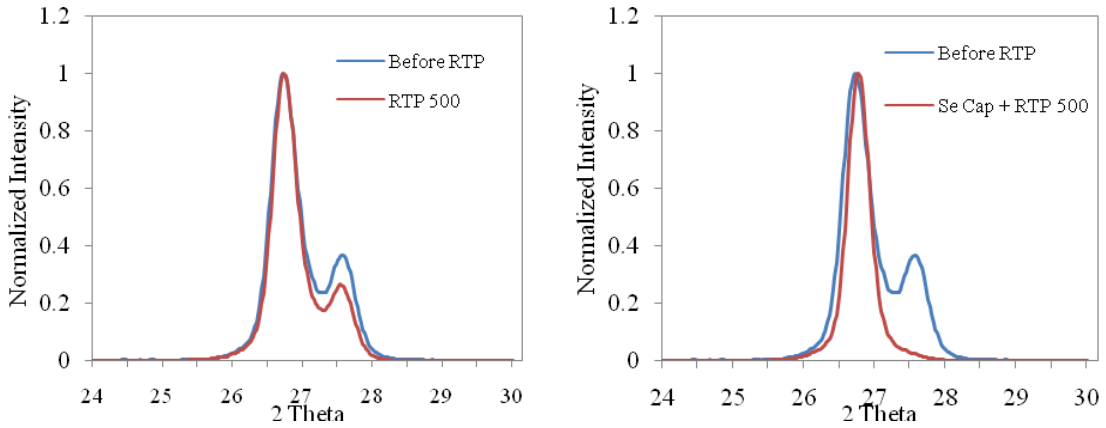

Figure 38. GIXRD patterns of (112) peaks from $(AgCu)(InGa)Se_2$ films before and after RTA treatment at 500°C in Ar and with an additional Se cap on the $(AgCu)(InGa)Se_2$. An unidentified peak at 27.6° was eliminated by the RTA treatment with extra Se.

XPS was used to further characterize the surface and help understand the unidentified XRD peak. The measurements were performed using a Physical Electronics instrument with a monochromatic Al Kα x-ray excitation under the applied voltage of 20 kV. An Ar^+ ion gun (2 keV) was used to perform depth profiling by etching layer by layer and analyzing the surface afterwards.

Figures 39 and 40 show XPS depth profile results on four samples with $x = 0.64$ and $w = 0$, 0.22, 0.74, and 1. The Ar etch rate was about 1 nm/min and the data was normalized with respect to the EDS bulk composition at the last measured etch time. The effect of preferential sputtering

has not been taken into account here so only relative differences are significant. In all films the Ga and In concentrations were uniform through the region probed and are not shown. Figure 39 shows the Se concentration for the four films. When the Ag content is low, there is higher Se near the surface while the films with high Ag content have concentration close to the stoichiometric values with little apparent depth dependence.

The variation of the ratio (Cu+Ag)/Se is shown in Figure 40. When $w = 1$ [$Ag(InGa)Se_2$] there is excess Ag near the surface. All other samples show (Cu+Ag) deficiency near the surface relative to the bulk. This deficiency develops by going from the bulk toward the surface, and the sample with the Ag/(Ag+Cu) ratio of 0.74 has the lowest Cu+Ag concentration. The XPS results revealed that when the Ag content is low (≤ 0.2), there is excess Se (more than stoichiometric values) and low Cu+Ag near the surface, consistent with the formation of an ordered vacancy compound that is normally observed at the surface of $Cu(InGa)Se_2$ films. The surface composition is different with higher Se as the unknown peak seen in the GIXRD develops. Lower Se in the surface of the higher Ag samples is consistent with the elimination of this peak when the films are annealed with an extra Se cap. However, the specific phase that corresponds to the XRD peak is still undetermined.

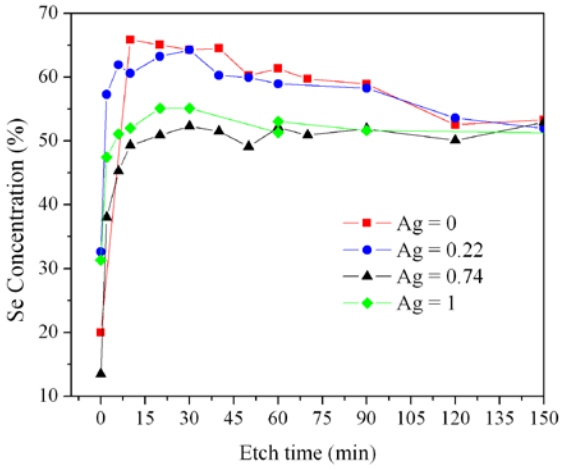

Figure 39. XPS depth profile of Se for alloys with Ga/(In+Ga) = 0.64 and various Ag/(Ag+Cu) ratios

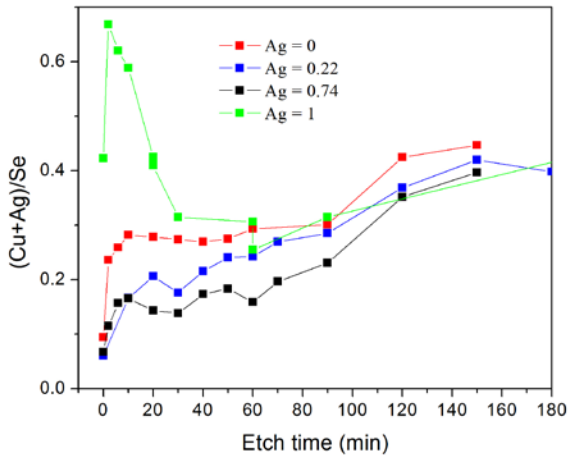

Figure 40. XPS depth profile of (Cu+Ag)/Se for alloys with Ga/(In+Ga) = 0.64 and various Ag/(Ag+Cu)

VIII. Summary

In this project "Novel Approaches to Wide Bandgap $CuInSe_2$-based Absorbers" the development of high performance wide bandgap solar cells based on thin film alloys of $CuInSe_2$ was pursued to relax constraints on module design and enable tandem solar cell structures.

The alloying of $Cu(InGa)Se_2$ with Ag to form $(AgCu)(InGa)Se_2$ was shown to give improved material properties and better device performance with increasing bandgap. A comprehensive characterization of optical, structural, and electronic properties of $(AgCu)(InGa)Se_2$ was completed over the compositional range $0 \leq [Ga]/[In+Ga] \leq 1$ and $0 \leq [Ag]/[Ag+Cu] \leq 1$. Evidence of improved material quality includes reduced sub-bandgap optical absorption, sharper bandtails, and increased grain size with Ag addition. The Ag alloying was shown to increase the range of bandgaps over which solar cells can be fabricated without any drop-off in performance to ~ 1.35 eV. With bandgap greater than 1.6 eV, in the range needed for tandem solar cells, $(AgCu)(InGa)Se_2$ gave higher efficiency than other $CuInSe_2$-based alloys. Laser and rapid thermal annealing processes were developed and shown to provide means to modify surface properties but no conditions were found that improve the performance of solar cells beyond that of the best devices without annealing.

A number of significant accomplishments were achieved. These include:

1. Single phase $(AgCu)(InGa)Se_2$ films were deposited over a wide range of compositions including some which gave multi-phase polycrystal samples as previously reported in the literature. This enables the full range of compositions of this material system to be considered for thin film solar cells.
2. Using a simple single-stage co-evaporation process, a solar cell with 17.6% efficiency using a film with bandgap = 1.3 eV was achieved, demonstrating the viability of $(AgCu)(InGa)Se_2$ for high efficiency devices.

3. Using a three-stage co-evaporation process for $(AgCu)(InGa)Se_2$ deposition a device with efficiency = 13.0 % and V_{OC} = 890 mV with J_{SC} = 20.5 mA/cm^2, FF = 71.3% was achieved. This surpasses the performance of other wide bandgap $CuInSe_2$-based solar cells.
4. Using both single-stage and three-stage processes, increasing Ag content in wide bandgap films (E_g > 1.5 eV) gave improved device performance even with increasing bandgap. The best cell performance for high V_{OC} cells is attained with both high Ga content, [Ga]/[In+Ga] ≈ 0.8, and high relative Ag content, [Ag]/[Ag+Cu] ≈ 0.8.
5. Lattice parameters for the $(AgCu)(InGa)Se_2$ system were determined over the full compositional range and it was shown that the system violates Vegard's law with evidence for a structural transformation with increasing Ag fraction.
6. Optical measurements of $(AgCu)(InGa)Se_2$ showed transmission of sub-bandgap light greater than 90% for $(AgCu)(InGa)Se_2$ films, greater than typical $Cu(InGa)Se_2$ films. This would be a critical advantage for use of $(AgCu)(InGa)Se_2$ as the top cell in a tandem device structure.
7. A complete quantification of the optical bandgaps of $(AgCu)(InGa)Se_2$ and determination of optical bowing parameters as a function of varying relative [Ga]/[In+Ga] and [Ag]/[Ag+Cu] was completed.
8. Transient photocapacitance measurements showed sharper optical bandtails or lower Urbach energies in $(AgCu)(InGa)Se_2$ than $Cu(InGa)Se_2$. This indicates lower alloy disorder which suggests a higher quality material.
9. Drive level capacitance measurements of $(AgCu)(InGa)Se_2$ devices showed lower free carrier concentrations than typical $Cu(InGa)Se_2$ films.
10. Characterization of metastable effects induced by light soaking of $(AgCu)(InGa)Se_2$ devices indicated low densities of deep defects and suggest a change in the recombination states that limit V_{OC}.
11. Current-voltage and quantum efficiency analysis indicated that V_{OC} in devices over the entire composition range is limited by Shockley-Read-Hall recombination in the absorber layer. The diode quality factor increases with Ga content suggesting recombination traps closer to mid-gap. Poor current collection was identified as an additional loss mechanism at wide bandgap, independent of the Ag content.
12. Surface characterization of $(AgCu)(InGa)Se_2$ films showed an unidentified phase on films with both high Ga and Ag concentrations that can be removed by annealing with excess Se.
13. Pulsed laser and rapid thermal annealing processes were developed and a range of parameters that could modify surface properties were determined. With both annealing methods, treatments could improve performance over control devices in some cases but the best overall performances were not exceeded.

Appendix I: Publications

1. "Characterization and Device Performance of (AgCu)(InGa)Se_2 Absorber Layers," Gregory M. Hanket, Jonathan H. Boyle, and William N. Shafarman, Proc. 34th IEEE PVSC, Philadelphia, PA, June 8-12, 2009.
2. "Optical and Quantum Efficiency Analysis of (Ag,Cu)(In,Ga)Se_2 Absorber Layers," Jonathan Boyle, Gregory Hanket and William Shafarman, Proc. 34th IEEE PVSC, Philadelphia, PA, June 8-12, 2009.
3. "Characterizing the Effects of Silver Alloying in Chalcopyrite CIGS Solar Cells with Junction Capacitance Methods," Peter T. Erslev, Gregory M. Hanket, William N. Shafarman, and J. David Cohen, Mater. Res. Soc. Symp. **1165,** 1165-M01-07 (2009).
4. "Device Characterization of (AgCu)(InGa)Se_2 Solar Cells," William Shafarman, Christopher Thompson, Jonathan Boyle, Gregory Hanket, Peter Erslev and J. David Cohen, Proc. 35th IEEE PVSC, Waikiki, Hawaii, June 21-25, 2010.
5. "Wide-bandgap (AgCu)(InGa)Se_2 Absorber Layers Deposited by Three-stage Co-evaporation," Gregory Hanket, Jonathan H. Boyle, William N. Shafarman, and Glenn Teeter, Proc. 35th IEEE PVSC, Waikiki, Hawaii, June 21-25, 2010.
6. "Structural characterization of the (AgCu)(InGa)Se_2 thin film alloy system for solar cells," J.H. Boyle, B.E. McCandless, G.M. Hanket, W.N. Shafarman, Thin Solid Films, to be published (2011).
7. "The electronic structure of Cu($In_{1-x}Ga_x$)Se_2 alloyed with silver," Peter T. Erslev, JinWoo Lee, Gregory M. Hanket, William N. Shafarman, J. David Cohen, Thin Solid Films, to be published (2011).
8. "Metastable properties of Cu($In_{1-x}Ga_x$)Se_2 with and without sodium" Peter T. Erslev, William N. Shafarman, and J. David Cohen, Appl. Phys. Lett. **98**, 062105 (2011).

<u>In Preparation</u>

1. "Optical properties of the (AgCu)(InGa)Se_2 thin film alloy system," J.H. Boyle, G.M. Hanket, W.N. Shafarman.
2. "Effect of rapid thermal annealing on wide bandgap Cu(InGa)Se_2 solar cells," H. Simchi, K. H. Kim, W.N. Shafarman.
3. "(AgCu)(InGa)Se_2 thin film solar cells," W.N. Shafarman, G.M. Hanket, and J.H. Boyle.
4. "Surface characterization of (AgCu)(InGa)Se_2 thin films for solar cells," H. Simchi, K. Kim, B. McCandless, W. Shafarman, and R. Birkmire, Proc. 37th IEEE Photovoltaic Specialists Conf., Seattle (2011).

Appendix II. Contributors

At IEC, University of Delaware

William Shafarman	Principal Investigator
Gregory Hanket	Research Associate
Erten Eser	Associate Scientist
Brian McCandless	Associate Scientist
Woo Kyoung Kim	Postdoctoral Research Associate
Kihwan Kim	Postdoctoral Research Associate
Christopher Thompson	Limited Term Researcher
Jonathan Boyle	Graduate Student, Materials Science and Engineering
James Wilson	Graduate Student, Materials Science and Engineering
Hamed Simchi	Graduate Student, Materials Science and Engineering
Dan Ryan	Senior Research Technician
Kevin Hart	Senior Research Technician

At University of Oregon

J. David Cohen	Principal Investigator
Peter Erslev	Graduate Student, Physics
JinWoo Lee	Graduate Student, Physics
Charles Warren	Graduate Student, Physics
David Miller	Graduate Student, Physics

At NREL

Glenn Teeter

References

i. W. Shafarman, S. Siebentritt, and L. Stolt, in *Handbook of Photovoltaic Science and Engineering, 2nd Ed.*, edited by A. Luque and S. Hegedus, (John Wiley & Sons, Ltd., London, 2011) pp. 546-599.

ii. R. Kniese, *et al*. in *Wide-Gap Chalcopyrites*, edited by S. Siebentritt and U. Rau (Springer, Berlin, Heidelberg, 2006) 235-254.

iii. T. Coutts et al., *Progress in Photov*. **11**, 359-375 (2003).

iv. J.L. Shay, J.H. Wernick, Ternary *Chalcopyrite Semiconductors: Growth, Electronic Properties, and Applications*, edited by B.R. Pamplin, (Pergamon Press, New York, 1975) pg 12, 118.

v. E. Ahmed et al., *J. Materials Eng. and Perf*. **15**, 213 (2006).

vi. H. Miyazaki et al., *Jap. J. Appl. Phys.* **43**, 4244 (2004).

vii. X. Wang et al., *Solar Energy Mat and Solar Cells* **88**, 65 (2005).

viii. A. Gabor, *et al*., *Sol. Energy Mater. Sol. Cells* **4**, 247 (1996).

ix. G. Hanket, J. Boyle, W. Shafarman, and G. Teeter, Proc. 35th IEEE PVSC, Waikiki, Hawaii, June 21-25, 2010.

x. M. Balboul, et. al. *J. Vac. Sci. Technol*. A **20**, 1247 (2002).

xi. J. Avon, K. Yoodee, and J. Woolley, *J. Appl. Phys*. **55**, 524 (1984).

xii. J. Boyle, B. McCandless, G. Hanket, and W. Shafarman, *Thin Solid Films*, to be published (2011).

xiii. M.U. Cohen, *Rev. Sci. Instrum.* **6**, 68(1935) ; **7**, 155 (1936).

xiv. C. Suryanarayana, M.G. Norton, *X-Ray Diffraction: A Practical Approach,* (Plenum Press, New York, NY, 1998) 159-164.

xv. J. Boyle, G. Hanket and W. Shafarman, Proc. 34th IEEE PVSC, Philadelphia, PA, June 8-12, 2009.

xvi. T. Colakoglu, M. Parlak, S. Oezder, *J. Non-Cryst. Solids* **354,** 3630 (2008).

xvii W. Shafarman, R. Klenk and B. McCandless, J. Appl. Phys. 79, 7324 (1996).

xviii R. Herberholz, et al., Solar En. Mat. and Solar Cells, 49, 227 (1997).

xix Young *et al.*, *Prog. Photovolt.* **11**, 535-541 (2003).

xx. Merdes, S. *et al.*, *Appl. Phys. Lett.* **95**, 213502 (2009).

xxi Shafarman, W. *et al. Proc. 29th IEEE Photovoltaic Specialist Conf*, 519 (2002).

xxii. G. Hanket, J. Boyle, and W. Shafarman, Proc. 34th IEEE PVSC, Philadelphia, PA, June 8-12, 2009.

xxiii. T. Nakada *et al.*, *Mater. Res. Soc. Symp. Proc.* **865**, 327 (2005).

xxiv S. Hegedus and W. Shafarman, Prog. in Photovoltaics 12, 155 (2004).

xxv J. Phillips, et al., Phys. Status Solidi B 194, 31 (1996).

xxvi C. Sah, R. Noyce and W. Shockley, Proc. Inst. Radio Engrs. 45, 1228 (1957).

xxvii C. Thompson, et al. Proc. 33rd IEEE PVSC (2008).

xxviii. C.E. Michelson, A.V. Gelatos, and J.D. Cohen, Appl. Phys. Lett. **47**, 412 (1985).

xxix. J.T. Heath, J.D. Cohen, and W.N. Shafarman, J. Appl. Phys. **95**, 1000 (2004).

xxx. J.D. Cohen and A.V. Gelatos, in *Advances in Disordered Semiconductors Vol I: Amorphous Silicon and Related Materials*, ed. by H. Fritzsche (World Scientific, Singapore, 1988), pp. 475-512.

xxxi. A.V. Gelatos, K.K. Mahavadi, and J.D. Cohen, Appl. Phys. Lett. **53**, 403 (1988).

xxxii. J.D. Cohen, J.T. Heath, and W.N. Shafarman, in *Wide Gap Chalcopyrites*, S. Siebentritt and U. Rau, eds. (Springer Series in Materials Science, Berlin, 2006) pp. 69-90.
xxxiii. J.T. Heath, J.D. Cohen, W.N. Shafarman, D.X. Liao and A.A. Rockett, Appl. Phys. Lett. **80**, 4540 (2002).
xxxiv. J.E. Avon, K. Yoodee, J.C. Woolley, J. Appl. Phys. **55**, 524 (1984).
xxxv. Adam Halverson, Shiro Nishiwaki, William Shafarman, and J. David Cohen, Proc. 4th World Conference on Photovoltaic Energy Conversion, (IEEE, 2006) pp. 364-367.